2019

Scale-Dependent Plasticity And Nanoindentation Creep Of Geologic Materials

Christopher Thom
University of Pennsylvania, cthom11@gmail.com

Scale-Dependent Plasticity And Nanoindentation Creep Of Geologic Materials

Abstract

Nanoindentation is a commonly used technique in materials science that allows for the determination of the mechanical properties (e.g. hardness, elastic modulus, and creep) of single crystals and polycrystalline aggregates, but it has been severely underutilized for the study of geologic materials. In this dissertation, we demonstrate the effectiveness of nanoindentation for measuring the rheological behavior of a wide range of geologic materials. For all materials tested, including single crystals, polycrystalline samples, and two different natural fault surfaces, we identify an 'indentation size effect,' whereby the strength of the material increases with decreasing size of the indent. We explore the implications of this size effect for the scale-dependent surface roughness of faults and the plastic deformation of asperities in Chapter 2, and extrapolate the size effect to the relatively large grain size of the mantle to predict the peak strength of oceanic lithosphere in Chapter 3. In Chapter 4, we investigate the effect of relative humidity on the room temperature deformation of quartz in order to constrain the physical mechanism that gives rise to time-dependent increases in the static friction of quartz rocks. Our results demonstrate that there is no effect of relative humidity on the yield stress or creep behavior of quartz, in stark contrast with observations from macroscopic friction experiments on quartz rocks that show a dramatic effect of humidity on friction. This contrast demonstrates that asperity creep, the canonical explanation of the increase in static friction with time, is incorrect. Finally, in Chapter 5, we present a detailed nanoindentation study of the hardness and long duration creep behavior of halite. We demonstrate that creep parameters derived from our nanoindentation tests, when properly treated, are in quantitative agreement and can be directly compared to creep parameters derived from more traditional experimental geometries. This dissertation demonstrates the utility of using nanoindentation to determine physical properties and rheological behavior of rocks and minerals.

Degree Type

Dissertation

Degree Name

Doctor of Philosophy (PhD)

Graduate Group

Earth & Environmental Science

First Advisor

David L. Goldsby

Keywords

creep, friction, nanoindentation, size effect, surface roughness

Subject Categories

Geology | Geophysics and Seismology | Mechanics of Materials

SCALE-DEPENDENT PLASTICITY AND NANOINDENTATION CREEP OF GEOLOGIC MATERIALS

Christopher A. THOM

A DISSERTATION
in
Earth and Environmental Science

Presented to the Faculties of the University of Pennsylvania
in
Partial Fulfillment of the Requirements for the
Degree of Doctor of Philosophy
2019

Supervisor of Dissertation:

Dr. David L. GOLDSBY
Associate Professor, Earth and Environmental Science

Graduate Group Chairperson:

Dr. Douglas J. Jerolmack
Professor, Earth and Environmental Science

Dissertation Committee:
David L. Goldsby, Associate Professor, Earth and Environmental Science
Douglas J. Jerolmack, Professor, Earth and Environmental Science
Alain F. Plainte, Professor, Earth and Environmental Science
Robert W. Carpick, Professor, Mechanical Engineering and Applied Mechanics

SCALE-DEPENDENT PLASTICITY AND NANOINDENTATION CREEP OF GEOLOGIC MATERIALS

"Are you sure nano is where you want to be?"

-Anonymous

"God made the bulk; surfaces were invented by the devil."

-Wolfgang Pauli

ACKNOWLEDGMENTS

I would first and foremost like to thank my adviser David Goldsby for taking me on as a student and providing me with the opportunities and guidance that have gotten me through my Ph.D. Without his efforts, I would not have been able to present this work. Thank you to my Ph.D. committee members for their input and expertise in many meetings throughout the past 4 $\frac{1}{2}$ years, particularly Rob Carpick, whose class inspired part of Chapter 2 of this dissertation. There are also many individuals outside of Penn whom I would like to thank for their guidance, collaboration, and encouragement along the way, including Emily Brodsky, George Pharr, Lars Hansen, and too many more to be named here. To all of the graduate students who have endured the 4th floor offices with me and who have always been there for happy hour or writing papers over a beer, I cannot thank you enough for making my time at Penn a positive experience. Hopefully we all cross paths again soon! Finally, I would like to thank my parents for always supporting me and for putting me onto the track I am on today. Without them, none of this would have been possible.

Funding support for my Ph.D. has been provided primarily through a Benjamin Franklin Fellowship from the University of Pennsylvania. Additional support was provided by NSF Grants EAR 1624504 and EAR 1550112 via my adviser, Professor David L. Goldsby. I also received travel support to attend conferences and to perform research at Argonne National Laboratory through the Greg and Susan Walker Endowment and student travel

grants from the Graduate and Professional Student Assembly (GAPSA) at the University of Pennsylvania.

ABSTRACT

SCALE-DEPENDENT PLASTICITY AND NANOINDENTATION CREEP OF GEOLOGIC MATERIALS

Christopher A. THOM

Dr. David L. GOLDSBY

Nanoindentation is a commonly used technique in materials science that allows for the determination of the mechanical properties (e.g. hardness, elastic modulus, and creep) of single crystals and polycrystalline aggregates, but it has been severely underutilized for the study of geologic materials. In this dissertation, we demonstrate the effectiveness of nanoindentation for measuring the rheological behavior of a wide range of geologic materials. For all materials tested, including single crystals, polycrystalline samples, and two different natural fault surfaces, we identify an 'indentation size effect,' whereby the strength of the material increases with decreasing size of the indent. We explore the implications of this size effect for the scale-dependent surface roughness of faults and the plastic deformation of asperities in Chapter 2, and extrapolate the size effect to the relatively large grain size of the mantle to predict the peak strength of oceanic lithosphere in Chapter 3. In Chapter 4, we investigate the effect of relative humidity on the room temperature deformation of quartz in order to constrain the physical mechanism that gives rise to time-dependent increases in the static friction of quartz rocks. Our results demonstrate that there is no effect of relative humidity on the yield stress or creep behavior of quartz, in stark contrast with observations from macroscopic friction experiments on quartz rocks

that show a dramatic effect of humidity on friction. This contrast demonstrates that asperity creep, the canonical explanation of the increase in static friction with time, is incorrect. Finally, in Chapter 5, we present a detailed nanoindentation study of the hardness and long duration creep behavior of halite. We demonstrate that creep parameters derived from our nanoindentation tests, when properly treated, are in quantitative agreement and can be directly compared to creep parameters derived from more traditional experimental geometries. This dissertation demonstrates the utility of using nanoindentation to determine physical properties and rheological behavior of rocks and minerals.

Contents

List of Figures

Chapter 1

Introduction

1.1 Dissertation Goal

The goal of this dissertation is to quantify the plastic deformation and creep behavior of geologic materials using nanoindentation, a technique which has been utilized for decades in materials science (e.g. Oliver and Pharr, 1992; Nix and Gao, 1998; Lucas and Oliver, 1999; Swadener, George, and Pharr, 2002; Oliver and Pharr, 2004; Pharr, Herbert, and Gao, 2010; Su et al., 2013; Ginder, Nix, and Pharr, 2018). Because of the high stresses needed to cause plastic deformation of geological materials at room temperature, very few experiments have been performed to study the low-temperature rheological behavior of rocks and minerals relevant to understanding the strength of the lithosphere. The main difficulty in deforming polycrystalline samples at large differential stresses is suppressing fracturing (e.g. Druiventak et al., 2011). Microfracturing can be suppressed by applying a large hydrostatic confining pressure, but the stresses required to deform minerals at low temperature are large, and therefore the level of confining pressure required to suppress fracturing is often effectively unreachable with current technology. Nanoindentation, however, offers the advantage that the sample itself acts as its own pressure vessel. Material surrounding the deforming volume deforms elastically and effectively confines the stressed region, suppressing fractures. Additionally, experiments can be performed at length scales small enough that plastic flow is more favorable than fracture. The relative

ease of performing nanoindentation experiments also makes it an attractive alternative for measuring the high-stress deformation of geologic materials. While nanoindentation is not a commonly used technique in geophysics, this dissertation will demonstrate its effectiveness in answering important questions about the plastic deformation and creep of geologic materials.

1.2 Brief History and Introduction to Nanoindentation

While nanoindentation did not become a widely used technique until the early 1990s (Oliver and Pharr, 1992), dead weight microindentation methods have existed and been used in geoscience for many decades (e.g. Brace, 1963; Hanneman and Westbrook, 1968; Evans and Goetze, 1979; Evans, 1984). The basic premise of microindentation relies on applying a known load to a sample, then optically measuring the area of the residual indent in an optical microscope to determine the hardness of the material post experiment. The hardness is then simply defined as the load divided by the contact area. While microindentation can be a useful technique for determining the properties of geologic materials, particularly at elevated temperatures (e.g. Evans and Goetze, 1979), some problems exist. Specifically, fracturing of the sample at the high loads typical of a microindentation test can cause problems with determining the hardness, and human error in measuring the size of an indent can result in significant systematic errors.

The invention of nanoindentation allowed for greater precision in the measurement of material properties, including the ability to determine the elastic modulus of the sample simultaneously with its hardness (Oliver and Pharr, 1992), without having to visually examine the residual indent. The details of this technique are discussed in greater detail later in this thesis, but the basic principles are outlined here. In a nanoindentation experiment, both the applied load and the penetration depth of the indenter into the sample are measured. This allows one to determine the contact stiffness, and using Sneddon's

solution (Sneddon, 1965), to determine the true depth at which the indenter and sample are in contact (Oliver and Pharr, 1992; Oliver and Pharr, 2004).). Using a depth-area relationship calibrated using known standards (usually fused silica), the contact area can be determined through measurement of the load and depth. The contact area, coupled with the known applied load, allow one to calculate the hardness of the material and also the elastic modulus (Oliver and Pharr, 1992; Oliver and Pharr, 2004). Improvements on this basic method have been introduced through the years. One important innovation is the development of the "continuous stiffness method" (CSM). Using this technique, an oscillation of the indenter tip force or displacement is introduced, and the corresponding phase lag in displacement or force, respectively, is measured. Using a dynamic model of the indenter system, this allows the contact stiffness to be determined at a frequency of $\sim$100 Hz (Li and Bhushan, 2002). The stiffness can then be used to calculate the contact area, elastic modulus, and the hardness. This method effectively eliminates the issue of thermal drift, which can plague hardness and creep measurements that are based on measured tip displacements. Using the CSM, the stiffness and ultimately the hardness are determined over timescales too small for thermal drift to be significant (e.g. Goldsby et al., 2004). Using the CSM also allows one to measure depth-dependent variations in hardness and other properties in a single indentation test. All of these techniques were utilized in this thesis and are described in more detail below.

1.3 Dissertation Structure

Plastic deformation occurs in a variety of geologic settings, including on asperities, which are geometrical protrusions on a fault surface that come into contact and determine its frictional behavior (e.g. Dieterich and Kilgore, 1994; Boettcher, Hirth, and Evans, 2007), and in the colder portions of the olivine-rich upper mantle in subducting oceanic slabs (e.g.

Kohlstedt, Evans, and Mackwell, 1995; Mei et al., 2010; Idrissi et al., 2016). Nanoindentation is able to effectively simulate a single asperity contact, making it a useful analogue for studying the deformation of fault surfaces. In Chapter 2, we quantify the scale-dependent strength of natural fault surfaces using nanoindentation, and directly compare the results to predictions inferred from measurements of roughness on the same faults. This comparison quantitatively links the geometry of faults, which exerts a fundamental control on frictional properties, to measurable material properties. In Chapter 3, we describe nanoindentation tests on olivine which reveal a scale-dependent yield strength. Microstructural analysis that has not been included in this dissertation suggests that the deformation in these nanoindentation tests is accommodated and limited by the same mechanisms as in polycrystalline samples deformed at low temperature. The extrapolation of our hardness results suggests that one may also expect a variation in the yield stress as a function of grain size, akin to a Hall-Petch strengthening mechanism (Hall, 1951; Petch, 1953; Dieter and Bacon, 1986). This potential variation of strength with grain size has not been previously considered for olivine. Taking this potential grain size effect into account appears to resolve discrepancies between experiments performed over the past 40 years. Additionally, extrapolation to mantle grain sizes can bring estimates of the peak strength of oceanic lithosphere from experimental, theoretical, and geophysical field work into closer quantitative agreement. Although it is not presented in this thesis, ongoing experimental work has confirmed this hypothesis set forth in Chapter 3 (Hansen, Thom, et al., manuscript in revision at *Journal of Geophysical Research*).

In addition to measuring plastic deformation, nanoindentation is also useful for measuring creep of geologic materials. A major open question in studies of rock friction and earthquake nucleation is whether the time-dependent increase in friction for two surfaces held in quasi-stationary contact, called frictional aging, is due to an increase in the real area of contact due to creep of asperities ("contact quantity") or due to an increase in the amount

of chemical bonding across the frictional interface ("contact quality"). The commonly accepted hypothesis is that creep of asperities is due to an increase in contact quantity caused by asperity creep (Dieterich and Kilgore, 1994; Marone, 1998; Scholz, 2002), but this result has not been directly shown in experiments for rocks. Interestingly, friction experiments in very low relative humidity conditions have demonstrated that frictional aging can be suppressed by the elimination of water from the system (Dieterich and Conrad, 1984; Frye and Marone, 2002), suggesting that the underlying mechanism of aging depends on water. Experiments are presented in Chapter 4 that were designed to test the creep behavior of quartz as a function of relative humidity at room temperature. These experiments are a strong test of predictions made by the "contact quantity" hypothesis of frictional aging. Our results demonstrate that the yield stress and creep behavior of quartz are independent of humidity, and thus the widely accepted "contact quantity" hypothesis cannot explain the suite of observations reported in the literature.

The final chapter of this dissertation, Chapter 5, directly compares the results of an extensive set of nanoindentation experiments on halite single crystals to flow laws derived from deformation experiments on polycrystalline halite samples at elevated temperature using more traditional deformation apparatus. Using a theoretical treatment of the data that allows nanoindentation creep data to be compared with uniaxial and triaxial tests on macroscopic samples (from Bower et al., 1993), we will show that our results show remarkable quantitative agreement with extrapolations of existing flow laws (e.g. Wawersik and Zeuch, 1986). This close quantitative agreement demonstrates that nanoindentation tests capture the same basic microphysical deformation mechanisms as more traditional experiments, justifying the use of nanoindentation as an additional and complementary method in the study of the deformation of geological materials.

Chapter 2

Scale-Dependent Roughness and Strength of Natural Fault Surfaces

A version of this chapter was previously published as: **Thom, C.A.**, Brodsky, E.E., Carpick, R.W., Pharr, G.M., Oliver, W.C., and Goldsby, D.L. (2017), Nanoscale roughness of natural fault surfaces controlled by scale-dependent yield strength. *Geophysical Research Letters* **44** (18), 9299-9307. doi:10.1002/2017GL074663

Abstract

Many natural fault surfaces exhibit remarkably similar scale-dependent roughness, which may reflect the scale-dependent yield strength of rocks. Using atomic force microscopy (AFM), we show that a sample of the Corona Heights Fault exhibits isotropic surface roughness well-described by a power law, with a Hurst exponent of 0.75 $\pm$ 0.05 at all wavelengths from 60 nm to 10μm. The roughness data and a recently proposed theoretical framework predict that yield strength varies with length scale as $\lambda^{-0.25\pm0.05}$. Nanoindentation tests on the Corona Heights sample and another fault sample whose topography was previously measured with AFM (the Yair Fault) reveal a scale-dependent yield stress with power-law exponents of -0.12 $\pm$ 0.06 and -0.18 $\pm$ 0.08, respectively. These values are within one to two standard deviations of the predicted value, and provide experimental

evidence that fault roughness is controlled by intrinsic material properties, which produces a characteristic surface geometry.

2.1 Introduction

Both natural and laboratory fault surfaces commonly exhibit well-defined, nominally flat, and highly reflective surfaces along which slip was localized. However, previous work has shown that topographic features are present at all length scales [Brown and Scholz, 1985; Power et al., 1987; Power, Tullis, and Weeks, 1988; Power and Tullis, 1991; Schmittbuhl, Gentier, and Roux, 1993; Lee and Bruhn, 1996; Power and Durham, 1997; Renard et al., 2006; Sagy, Brodsky, and Axen, 2007; Candela et al., 2009; Candela et al., 2011; Brodsky et al., 2011; Candela et al., 2012; Renard, Mair, and Gundersen, 2012; Renard, Candela, and Bouchaud, 2013; Candela and Brodsky, 2016; Brodsky, Kirkpatrick, and Candela, 2016], with the observed roughness varying as a function of both the measurement length and the resolution of the measurement technique. If a rough surface is described by a fractal geometry, for a change in lateral length scale, γ, an additional parameter called the Hurst exponent, ζ, is required to properly scale the vertical topography with the length scale of observation (i.e. $\delta x \rightarrow \gamma\delta x$ or $\delta y \rightarrow \gamma\delta y$ in lateral directions in the nominal x-y plane of the fault and $\delta z \rightarrow \gamma^{\zeta}\delta z$ in the z-direction perpendicular to the nominal plane of the fault). Recent high-resolution data from studies of roughness that average large quantities of digital data concluded that many fault surfaces exhibit a self-affine fractal geometry ($0 < \zeta < 1$) over several orders of magnitude in lateral length scale ranging from microns to meters, with values of $\zeta \approx 0.6$ for profiles measured parallel to the slip direction (in the x-direction) and $\zeta \approx 0.8$ for profiles measured perpendicular to slip (in the y-direction) [e.g. Candela et al., 2012; Brodsky, Kirkpatrick, and Candela, 2016]. We note that smaller values of ζ ranging from 0.2 to 0.5 have also been reported [e.g. Tisato et al., 2012; Chen et al., 2013; Pluymakers, Kobchenko, and Renard, 2017]. However, arguments from contact mechanics

suggest that the Hurst exponent should typically lie in the range 0.7-1.0 to keep the surface inherently stable at all length scales [Persson, 2014]. If the surface geometry is self-affine ($0 < \zeta < 1$) rather than self-similar ($\zeta = 1$), the average aspect ratio (i.e., the ratio of height to width) of an asperity increases with decreasing length scale [Brodsky, Kirkpatrick, and Candela, 2016]. Remarkably, at a given length scale, there appears to be little variability in the measured spectral power of fault roughness, despite significant differences in the lithologies and slip histories of faults, suggesting that a common mechanism may control the surface geometry.

Previous studies of the surface topography created by tensile fractures have made similar observations about roughness, finding values of the Hurst exponent between 0.5 and 0.9, with values that vary with the orientation of the profile relative to the direction of crack propagation [e.g. Bouchaud and Navéos, 1995; Bouchaud, 1997; Ponson et al., 2006; Ponson, Bonamy, and Bouchaud, 2006]. These observations were explained by a number of models, including percolation of damage from a crack front, the coalescence of plastic voids, and depinning instabilities at the crack front [Hansen and Schmittbuhl, 2003; Bouchbinder, Mathiesen, and Procaccia, 2004; Bonamy and Bouchaud, 2011]. Unfortunately, none of these theories predicts the specific values of the Hurst exponents observed in fracture experiments. Furthermore, the shear surfaces studied here are affected by the cumulative shearing and wear that occurs during successive slip events and are not directly explainable by models of the propagation of a single tensile fracture. A more likely mechanism to produce fault roughness is the frictional sliding that occurs along fault surfaces, which can create and remove topographic features over a wide range of length scales.

Brodsky, Kirkpatrick, and Candela, 2016 hypothesized that the scale-dependent surface roughness of faults is a manifestation of scale-dependent material strength. These authors argue that asperities yield at a critical aspect ratio, which is related to a critical strain that varies with length scale. If the critical strain is exceeded, then the asperity will fail inelastically. This hypothesis is easily tested at small length scales using atomic force

microscopy (AFM) and nanoindentation to measure surface roughness and hardness, respectively, of the same fault surface.

Scale-dependent strength has been observed for many engineering materials and for brittle failure of rocks [e.g. Bandis, Lumsden, and Barton, 1981; Andreev, 1995; Uchic et al., 2004; Greer, Oliver, and Nix, 2005; Pharr, Herbert, and Gao, 2010], but has been much less studied at small scales in geologic materials where plastic deformation may dominate [Candela and Brodsky, 2016]. In the brittle regime, scale-dependent strength is often attributed to the statistical distribution of flaws, with an increasing likelihood of intersecting a flaw with increasing size of the deforming volume [Paterson and Wong, 2005]. Engineering studies show that at smaller scales, dislocation-based mechanisms may lead to scale-dependent plastic strength. The indentation size effect, in which the measured indentation hardness of a material increases with decreasing indentation size, is a well-known example [e.g. Bull, Page, and Yoffe, 1989; Nix and Gao, 1998; Swadener, George, and Pharr, 2002; Durst, Backes, and Göken, 2005; Pharr, Herbert, and Gao, 2010]. This effect is often attributed to strain gradients that develop in the vicinity of the indenter tip, with highly deformed material in close proximity to undeformed, comparably less-stressed regions [Nix and Gao, 1998]. Smaller indents are thought to result in a higher density of dislocations under the indenter tip, which are known as geometrically necessary dislocations [Nye, 1953], compared to the background dislocation density. This increased density causes interactions between dislocations that leads to a strengthening effect and an increase in the measured indentation hardness, which is proportional to yield stress. In polycrystalline materials, the Hall-Petch effect is another size-dependent strength phenomenon whereby the yield strength increases with decreasing grain size [Hall, 1951; Petch, 1953; Dieter and Bacon, 1986]. Some authors have recently argued that the indentation size effect and Hall-Petch strengthening are different manifestations of a general size-strength effect [Li, Bushby, and Dunstan, 2016]. These studies demonstrate that a variety of mechanisms make scale-dependent strength an expected, but insufficiently quantified, feature of

rock deformation.

Here, we investigate the potential link between scale-dependent plastic strength and fault roughness at nanometer length scales, using AFM to measure small-scale roughness and nanoindentation to measure indentation size effects for natural fault surfaces. In Section 2.3, we demonstrate that the Corona Heights Fault exhibits a characteristic roughness well-described by a power law at nanometer to micron length scales. This power-law scaling of roughness, coupled with Brodsky, Kirkpatrick, and Candela, 2016's hypothesis described above, predicts a specific value of the exponent in a power-law relationship between yield strength and length scale. We next show that the yield strength of two natural fault surfaces is scale-dependent, with values of the power-law exponent that fall within one to two standard deviations of the predicted value based on fault roughness measurements. We present an interpretation of our results in Section 2.4 before exploring the implications of scale-dependent roughness and yield strength for natural and laboratory faults in Section 2.5.

2.2 Methods

2.2.1 Roughness Measurements Using Atomic Force Microscopy

The topography of a small area ($\sim$1 cm^2) of the Corona Heights Fault was measured in a Bruker Icon AFM operating in intermittent contact mode [see Appendix A] with a maximum scan length of 10 μm. Figure 2.1 shows a photograph of the fault exposure, a hand sample collected at the site, and an example of the topographic data collected via AFM. The power spectral density, a measure of the amplitude of the roughness contributed at each wavelength, can be calculated via a number of methods, each with its own degree of bias [Schmittbuhl, Schmitt, and Scholz, 1995; Schmittbuhl, Vilotte, and Roux, 1995; Candela et al., 2009; Jacobs, Junge, and Pastewka, 2017]. We determined the power spectral density of 2-D profiles by calculating the Fourier transform of the autocorrelation function

and normalizing by the profile length, consistent with the work of several previous authors [see Appendix A; Candela et al., 2009; Candela et al., 2011; Renard, Mair, and Gundersen, 2012; Renard, Candela, and Bouchaud, 2013; Brodsky, Kirkpatrick, and Candela, 2016]

2.2.2 Hardness Measurements Using Nanoindentation

Two fault surfaces, the Corona Heights Fault and the Yair Fault, were indented in a manner designed to reveal indentation size effects. Initial tests on the Corona Heights Fault showed scatter in the indentation data due to the significant roughness of the sample. To minimize roughness effects on the hardness measurements, the surface was lightly polished with 5 micron grit on a wet felt polishing wheel to create a smoother, more uniform topography, which resulted in cleaner, less scattered data. The Yair Fault, a dolomitic 'mirror' surface whose roughness was previously characterized by AFM [Siman-Tov et al., 2013], was not polished or otherwise altered prior to the indentation tests. The Yair Fault sample also exhibits multiscale roughness over several orders of magnitude in length scale, quantitatively similar to that measured for Corona Heights in this paper (see below), despite a significant difference in mineralogy (carbonate for Yair and silica-rich for Corona Heights). That the topography is similar for the vastly different mineralogies of the two faults suggests that some common process(es) controls the surface roughness.

Nanoindentation tests were conducted in an iMicro Nanoindenter (Nanomechanics, Inc.) using the continuous stiffness method to determine the hardness and elastic modulus of the two fault surfaces as functions of indentation depth [see Appendix A; Oliver and Pharr, 1992; Li and Bhushan, 2002; Oliver and Pharr, 2004]. Experiments were performed with a diamond Berkovich tip indenting at a nominally constant strain rate (i.e., at a constant ratio of $\dot{P}/P$, where P is the normal load on the indenter tip and $\dot{P}$ is its time derivative) of 0.2 s^{-1}. To convert hardness to yield stress, we calculated the constraint factor for a sharp tip geometry such as the Berkovich [see Appendix A; Johnson, 1970; Evans and Goetze, 1979].

2.3 Results

2.3.1 Nanoscale Fault Roughness

Power spectral density curves from all roughness measurements are plotted in Figure 2.2, with profiles measured parallel to the direction of slip, as indicated by slickenlines on the fault surface, shown in purple, and profiles measured perpendicular to slip shown in green. All spectra, both those scanned parallel to and perpendicular to the slip direction (i.e., in the x- and y-directions), display limited variability of power spectral density, indicating that the surface is isotropic at these small scales. Because of the isotropic nature and limited variability of the roughness data, all spectra shown in Figure 2.2 were averaged together, with the average shown by the thick black curve.

We observe a linear relationship between power spectral density and wavelength, λ, on log-log axes, which can therefore be fit with a power law. In order to facilitate comparison with previous studies, we cast the exponent of that power law in terms of the Hurst exponent, ζ, which can be directly calculated from the slope of the line, α, by

$$\zeta = \frac{(\alpha - 1)}{2} \tag{2.1}$$

Note that because of the limited scale-range of this study, we make no specific claims about self-affinity, but merely utilize the previously-established power-law functional form to have a mathematical basis for comparison between roughness, hardness, and the results of previous work. Figure 2.2 also shows a best-fit line (in blue) to the averaged data with α = 2.5 $\pm$ 0.1, where the error bars represent one standard deviation. This gives a value of ζ = 0.75 $\pm$ 0.05, in agreement with the value of 0.8 observed perpendicular to slip at larger length scales (up to several meters) on several other faults [Candela et al., 2012]. Figure A.1 shows a histogram of the Hurst exponents derived from fitting a power law to each individual spectrum shown in Figure 2.2, and is in agreement with the average value

reported above. Here, the roughness can be well-described by a single power law down to a wavelength of 60 nm, with no discernible small-scale cutoff or change in slope. This clear, unchanging power-law trend differs from the trend presented in Siman-Tov et al., 2013 on the Yair Fault, which showed a continuously varying value of the Hurst exponent. However, much of the observed change in the roughness scaling in Siman-Tov et al., 2013 is at small wavelengths (< 50-100 nm). At these length scales, it has been recently shown that artifacts caused by the finite size of the AFM tip can become significant [Jacobs, Junge, and Pastewka, 2017]. At larger length scales, a single Hurst exponent appears to adequately describe the roughness of the Yair Fault, in agreement with our observations for the Corona Heights Fault.

When $0 < \zeta < 1$, the aspect ratio of asperities on the fault surface increases with decreasing wavelength. The average asperity height, h, changes with its wavelength, λ, according to

$$h \propto \lambda^{\zeta} \tag{2.2}$$

so that the aspect ratio, h/λ, changes as

$$\frac{h}{\lambda} \propto \lambda^{\zeta-1} \tag{2.3}$$

The ratio $\frac{h}{\lambda}$ is essentially equivalent to the RMS slope of the surface [Hyun et al., 2004; Pei et al., 2005]. Larger wavelength asperities have smaller aspect ratios according to our measured value of the Hurst exponent (0.75 +/- 0.05) for length scales from 60 nm to 10 μm, consistent with observations at larger scales. If this characteristic roughness is controlled by an inherent scale-dependent material strength, we might expect to observe an indentation size effect with a similar scaling relationship. This expectation derives from the hypothesis that the aspect ratio of an asperity reflects the critical strain at failure, which is proportional to the yield stress [Brodsky, Kirkpatrick, and Candela, 2016]. The indentation size effect describes how indentation hardness, which is proportional to yield

stress, changes with the size of the indent. Since we observe a value of $\zeta = 0.75 \pm 0.05$ for Corona Heights, we thus predict that its yield stress would scale with length scale as $\lambda^{-0.25\pm0.05}$. For the Yair Fault, Siman-Tov et al., 2013 found a surface topography similar to that for Corona Heights over the same range of length scales, suggesting that a similar scale-dependent yield stress may exist for the Yair Fault, but these authors did not report a fit to their roughness data. Using Siman-Tov et al., 2013's data for length scales of 60 nm to 10 μm (and thus avoiding instrumental artifacts as we have done in this study), we estimate that $\zeta = 0.7 \pm 0.1$, consistent with our Corona Heights data.

2.3.2 Scale-Dependent Yield Stress

f Residual indents were examined in an optical microscope and a scanning electron microscope to assess the degree of fracturing associated with the indents. No cracks associated with the indents were observed via either observation method, suggesting that the indentation strain was accommodated primarily via plastic deformation.

Figure 2.3 shows yield stress data for 35 indentation tests on the Corona Heights Fault and 7 tests on the Yair Fault. For Corona Heights, data from 4 individual tests are highlighted in color as examples, with data from the remaining tests shown in grey. Each test on the Yair fault is represented by a different color in Figure 2.3. Yield stress decreases with increasing indentation depth, in agreement with the prediction from the relationship between roughness and length scale, and with observations of indentation size effects in other materials [Pharr, Herbert, and Gao, 2010].

Data from individual tests were each fit to determine the value of the exponent in a power-law relationship between length scale and yield stress. For the Corona Heights Fault, we observe a power-law decay of yield strength with indentation depth with an average exponent of -0.12 $\pm$ 0.06. For the Yair Fault, we observe an exponent of -0.18 $\pm$ 0.08. For both values, the error bars represent one standard deviation. In Figure 2.3, solid-colored lines are fit to the yield stress vs. depth data to reveal the scale-dependence.

A histogram to demonstrate the variability of the derived power-law exponents for the Corona Heights Fault is shown in Figure A.2.

2.3.3 Complicating Factors in Nanoindentation Tests

Small-scale roughness and tilt of the sample surface are known to cause experimental artifacts during nanoindentation and in extreme cases lead to asymmetric indents [Kashani and Madhavan, 2011]. All data associated with visibly asymmetric indents due to local tilt of the sample surface were discarded. Although we attempted to minimize the effects of surface roughness by lightly polishing the Corona Heights sample, the surface still retained significant small-scale roughness after polishing, as evidenced by the non-reflective nature of the surface. These small-scale variations in surface topography likely contribute to the remaining scatter observed in the data.

In addition to roughness, the heterogeneous mineralogy and microstructure of the Corona Heights Fault surface likely contributes to the overall variability observed in the nanoindentation tests. The 0.5 to 3 mm thick translucent layer on the fault surface is composed of quartz, other silica phases, and iron oxide [Kirkpatrick et al., 2013]. Heterogeneity on length scales of order the size of the indents is present, and may lead to variations in hardness. Similar heterogeneity in the Yair Fault likely exists at these scales, although no detailed microstructural analyses have been made.

2.4 Interpretation

2.4.1 Consistency of Roughness Scaling and Yield Stress

Our results for the Corona Heights Fault suggest that fault roughness may be controlled by scale-dependent plastic yield strength, as proposed by Brodsky, Kirkpatrick, and Candela, 2016. The predicted scaling relationship derived from the roughness of a natural fault suggests that yield strength should decrease with length scale as a power-law with an

exponent of 0.25 $\pm$ 0.05. The nanoindentation data for Corona Heights reveal a value of the power-law exponent within approximately two standard deviations of the predicted value. Nanoindentation data for the Yair Fault show significantly less scatter compared to Corona Heights, with a value of the power-law exponent within one standard deviation of the predicted value.

2.4.2 Consistency of Roughness Amplitude and Yield Stress

Nearly all natural and engineered surfaces are rough over some range of length scales. The friction force between two surfaces is directly proportional to their real area of contact, highlighting the first-order control of surface roughness on friction [Bowden and Tabor, 1954]. Because the real area of contact is a small fraction of the nominal area of contact, stresses acting on asperities in contact are usually inferred to be large enough to induce plastic deformation. If a characteristic roughness has been obtained, the distribution of contact pressures acting on asperities should reflect the variability of the size and yield strength of asperities.

Elastic contact theories developed for rough surfaces over the past several decades provide constraints on the contact pressure on asperities [Greenwood and Williamson, 1966; Bush, Gibson, and Thomas, 1975; Persson, 2001]. Collectively, the contact theory of Persson [Persson, 2001; Persson, 2006; Persson, 2014] and the extensive numerical simulations of Hyun et al., 2004 and Pei et al., 2005 provide the most comprehensive model, as they incorporate roughness at all possible wavelengths within adjustable upper and lower bounds by using the power spectral density to determine a critical parameter, <*dh/dx*>, the RMS slope of a self-affine surface. Since a power law fits the data here to scales as small as 60 nm with a very similar value of the exponent to that observed in previous work, we utilize a self-affine model to help interpret the data. In this model, the mean elastic contact pressure on all asperities, P_m, is given by

$$P_m = \frac{E' \cdot \frac{dh}{dx}}{\kappa} \tag{2.4}$$

where E' is the reduced Young's modulus of the material (equal to $E/(1-\nu^2)$), where E is the Young's modulus and ν is Poisson's ratio), $\langle dh/dx \rangle$ is the RMS slope, and κ is a constant. The exact value of κ varies only slightly with Poisson's ratio and the Hurst exponent Hyun et al., 2004. We adopt a value of κ = 2.2, which Hyun et al., 2004 suggest is within 10% error for all surface geometries tested in their finite element simulations of contact between rough surfaces.

For the Corona Heights sample, we use the value of Young's modulus determined by nanoindentation (93 $\pm$ 3 GPa) and the calculated value of the RMS slope from the AFM data (0.26) at wavelengths of 60 nm to 10 μm [see Appendix A] to show that the average contact pressure on asperities is 11.0 $\pm$ 0.3 GPa. Error bars here represent one standard deviation and reflect the uncertainty in Young's modulus. This value is slightly larger than the yield stress of the Corona Heights Fault determined at indentation depths of 200-300 nm, suggesting that asperities are supporting stresses greater than or near their yield stress. The yield stress may continue to increase at smaller scales (< 200 nm), but we do not have nanoindentation data at these scales due to experimental limitations. Our data suggest that both the yield stress calculated from nanoindentation and the mean pressure calculated from contact mechanics for the Corona Heights Fault at these scales are approximately 10% of the Young's modulus, i.e., near the ideal strength.

It is important to note that only roughness data from wavelengths of 60 nm to 10 μm were included in the above calculation of RMS slope in order that this range of length scales would be directly comparable to the range of indentation depths studied, neglecting several orders of magnitude of roughness at larger scales. However, for surface roughness with a Hurst exponent less than 1, the roughness at the smallest length scale is the determining factor for the mean pressure, as it directly depends on the RMS slope, which increases at progressively smaller length scales [Hyun et al., 2004; Pei et al., 2005; Jacobs, Junge, and Pastewka, 2017]. Thus, neglecting large-scale roughness will not change the estimated mean pressure significantly. A more important detail, the lack of an observed

small-scale cutoff in the power-law scaling, has a greater impact on the RMS slope and mean pressure. Atomic force microscopy cannot resolve all roughness details, so roughness may exist at length scales smaller than our resolution of 60 nm. Therefore, our calculations may slightly underestimate the average contact pressure on asperities. We cannot obtain reliable AFM data at smaller length scales.

2.5 Implications for Scaling Roughness from the Laboratory to the Field

This study has shown that nanoscale surface roughness and plastic yield strength have compatible length scale-dependencies within one to two standard deviations. Our data support the assertion that a natural fault surface evolves to a steady-state roughness that is controlled by its intrinsic material strength. This framework has at least two important geological implications: (1) Fault roughness is expected to have limited variability over a wide range of pressure and temperature conditions in the Earth's crust. Earthquake dynamics models can benefit from the predictable nature of roughness derived from bulk material properties. (2) The scale-dependent strength of rocks can be inferred from a relatively straightforward measurement, the roughness of faults. This implication extends beyond geology and may have applications in other fields such as materials science and tribology. Shearing experiments may present a new way to examine the scale-dependent plastic strength of materials.

An important caveat is that in this study we focused only on nanoscale surface roughness and plastic deformation at small, micron to sub-micron scales because these are the scales for which roughness and yield strength data can be easily obtained. A similar scaling relationship between roughness and length scale exists at larger scales on natural faults, but the underlying mechanism by which it occurs has not been determined. Due to the

necessarily restricted size of most laboratory samples, a large wavelength cutoff of roughness is imposed by either machining and/or polishing, or by the physical dimensions of the sample. Mechanisms that result in this larger-scale roughness may not be revealed in laboratory tests, even though they may play an important role in earthquake nucleation and rupture behavior. Identification of mechanisms that cause roughness at these larger length scales is an important area of future research.

2.6 Conclusion

We have examined a sample of the Corona Heights Fault and shown that it exhibits isotropic surface roughness that is well-described by a power law, with a Hurst exponent of 0.75 $\pm$ 0.05, at length scales ranging from 60 nm to 10 μm. With the inclusion of data from this study, the Corona Heights Fault has now been shown to display consistent roughness scaling in the slip-perpendicular direction over nearly 9 orders of magnitude in lateral length scale [Candela et al., 2012; Candela and Brodsky, 2016], suggesting that some process(es) controls the observed roughness [Brodsky, Kirkpatrick, and Candela, 2016]. Nanoindentation tests performed on two natural faults, the Corona Heights and Yair Faults, reveal a scale-dependent yield strength, with yield strength increasing with decreasing size of the indents. The magnitude of this size effect for the Corona Heights Fault is described by a power-law between yield strength and length scale, with an exponent of -0.12 $\pm$ 0.06. For the Yair Fault, this size effect is described with an exponent of -0.18 $\pm$ 0.08. The magnitude of the size effect for the Corona Heights Fault, as reflected in the value of the power-law exponent, is within two standard deviations of the value of -0.25 $\pm$ 0.05 predicted from fault roughness, suggesting that roughness may be the result of scale-dependent yield strength. The data for the Yair Fault are in even better agreement, with the value of the power-law exponent for the size effect falling within one standard deviation of the value predicted from roughness.

Because scale-dependent yield strength is an inherent material property, a characteristic roughness results after some wearing-in of the fault surface. This characteristic roughness sets the size distribution and spatial correlation of asperities on fault surfaces, which ultimately controls frictional behavior and the nucleation of unstable slip. While we have focused on scale-dependent plastic yield strength, a similar mechanism may occur for brittle deformation at length scales larger than those investigated in this study, leading to grooving and the slip-orientation-dependent self-affine geometry measured on many faults. In addition, it should be noted that the nanoindentation experiments discussed here were conducted without shear loading, which may influence the yielding of asperities on faults loaded in shear. Failure during slip or interseismic loading may thus deviate from the deformation observed here during indentation. Despite these caveats, however, our results clearly demonstrate that scale-dependent strength exists for two natural fault surfaces, and suggest that future studies of fault friction may benefit from considering the effects of scale-dependent material strength.

2.7 Acknowledgments

The authors would like to acknowledge support from National Science Foundation awards EAR 1624504 and DMR 1427812. K. Johanns provided valuable guidance in conducting nanoindentation experiments and M.O. Robbins provided useful discussions. C. Marone and A. Sagy greatly helped to clarify and improve this paper through their careful and thoughtful reviews. All data used in this study are available at
`https://upenn.box.com/s/pqq1kyf5jiga8ow2cbi7qad87bnfzdy7`.

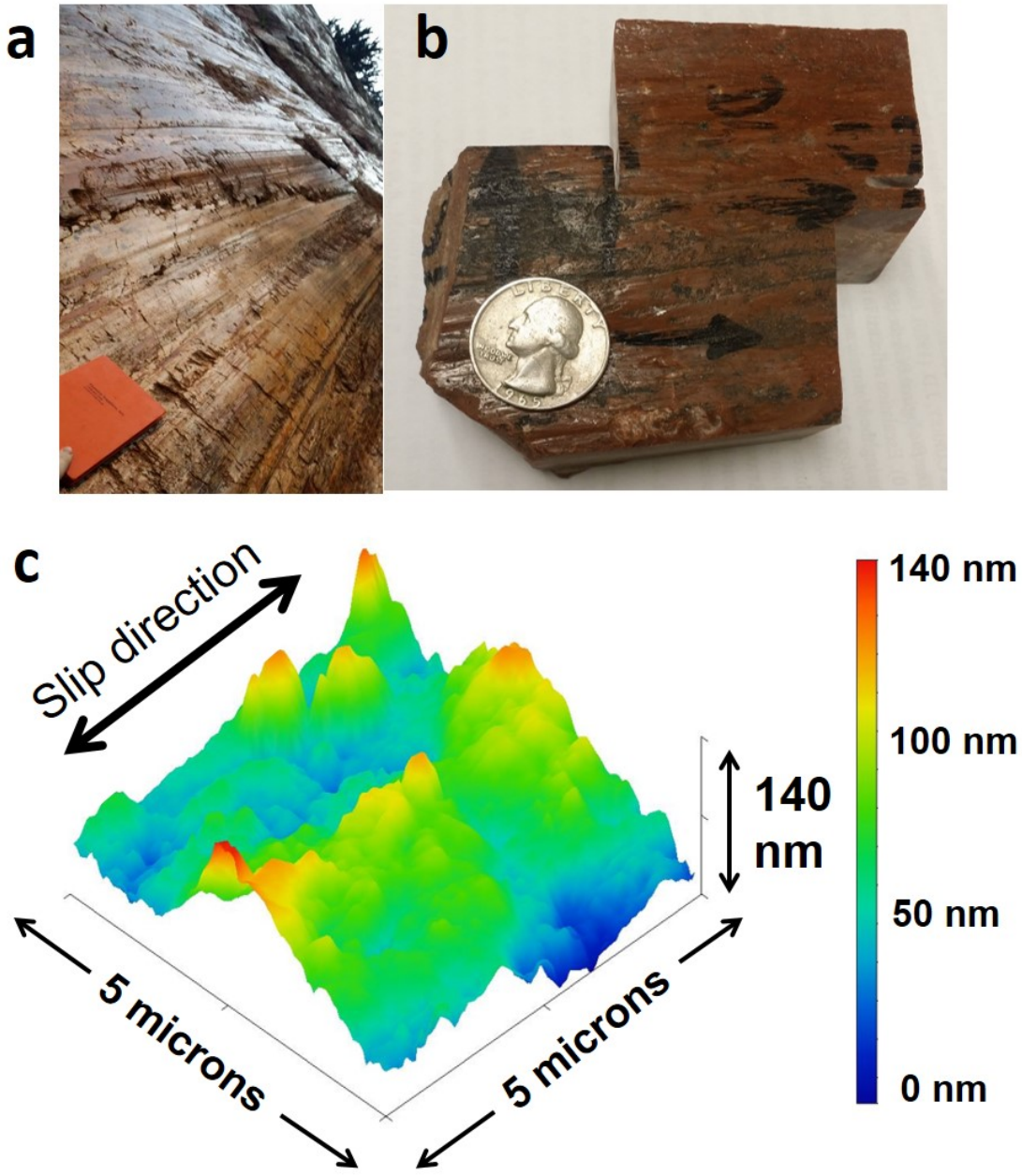

FIGURE 2.1: Photographs of **(a)** the exposure of the Corona Heights Fault in San Francisco, CA and **(b)** a hand sample collected from the fault. **(c)** Topography of a 5 by 5 micron portion of the surface collected via atomic force microscopy. Note that **(c)** has been greatly vertically exaggerated.

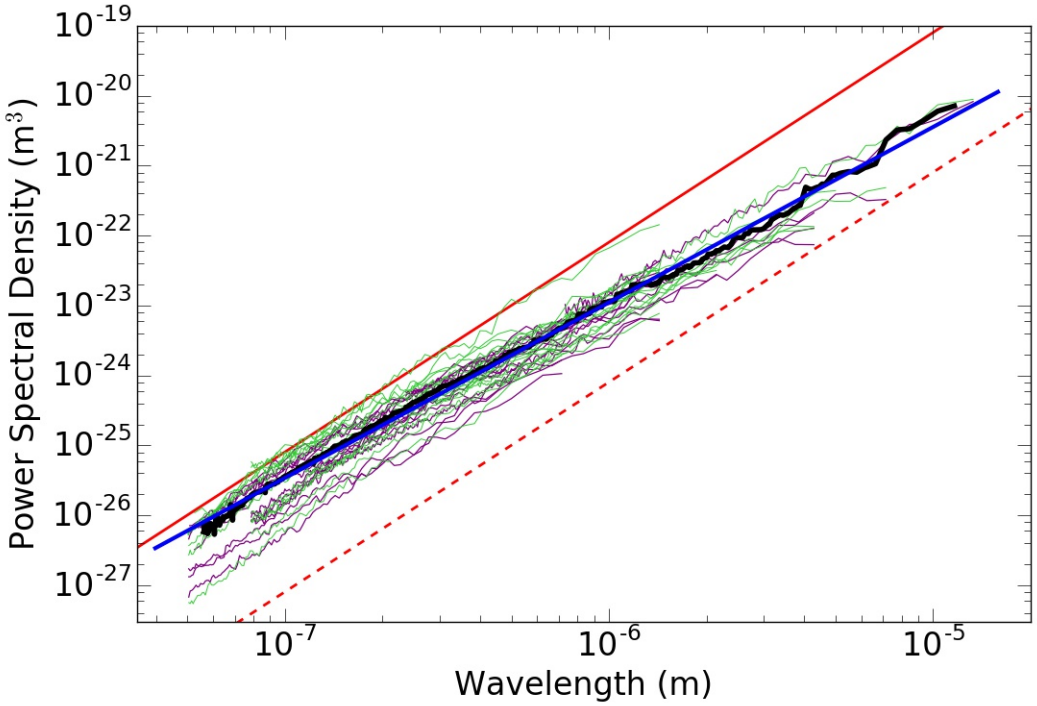

FIGURE 2.2: Power spectral density as a function of wavelength for slip-parallel and slip-perpendicular profiles, shown in purple and green, respectively, for the Corona Heights sample. The thick black line is an average of all data. The solid blue line is a linear fit to the averaged data with a slope of 2.5 ± 0.1. Constant asperity aspect ratios of 1% and 10% are represented by the dotted and solid red lines, respectively. The average power spectral density curve cuts across lines of constant aspect ratio, with larger aspect ratios occurring at smaller wavelengths.

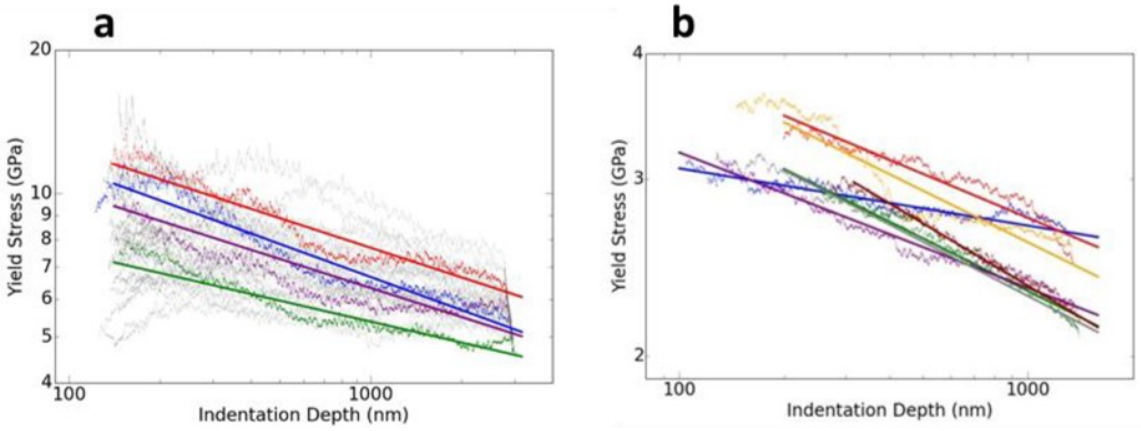

FIGURE 2.3: Yield stress as a function of indentation depth for **(a)** Corona Heights and **(b)** Yair Faults. In each diagram, the yield stress data, derived from the hardnesses determined from the continuous stiffness measurements, are presented as discrete data points, which appear as continuous traces due to the high density of data points. For Corona Heights, four tests are highlighted in color and the others are in grey. Solid-colored straight lines show the best fit to the corresponding data plotted in the same color in both **(a)** and **(b)**.

Chapter 3

Size Effects Resolve 40 Years of Work on Olivine Plasticity

A version of this appendix was previously published as: Kumamoto, K., **Thom, C.A.**, Wallis, D., Hansen, L.N., Armstrong, D.E.J., Warren, J.M., Goldsby, D.L., and Wilkinson, A.J. (2017), Size effects resolve discrepancies in 40 years of work on olivine plasticity. *Science Advances* **3**, e1701338. doi:10.1126/sciadv.1701338

Abstract

The strength of olivine at low temperatures and high stresses in Earth's lithospheric mantle exerts a critical control on many geodynamic processes, including lithospheric flexure and the formation of plate boundaries. Unfortunately, laboratory-derived values of the strength of olivine at lithospheric conditions are highly variable and greatly disagree with those inferred from geophysical observations. Here we demonstrate via nanoindentation that the strength of olivine depends on the length-scale of deformation, with experiments on smaller volumes of material exhibiting larger yield stresses. This "size effect" resolves discrepancies among previous measurements of olivine strength using other techniques. It also corroborates the most recent flow law for olivine, which proposes a much weaker lithospheric mantle than previously estimated, thus bringing experimental measurements

into closer alignment with geophysical constraints. Further implications include an increased difficulty of activating plasticity in cold, fine-grained shear zones, and an impact on the evolution of fault surface roughness due to the size-dependent deformation of nanometer- to micrometer-sized asperities.

3.1 Introduction

The strength of the lithospheric mantle, the relatively cold and rigid outer layer of the mantle, during deformation by low-temperature plasticity controls a range of geological phenomena, as the mantle comprises up to ∼95% of tectonic plates. For instance, lithospheric-scale strain localization, a necessity for the formation and longevity of plate boundaries, is primarily accommodated by plastic deformation of olivine [Thielmann and Kaus, 2012], the dominant mineral of the upper mantle. Low-temperature plasticity of olivine is also critical in lithospheric flexure beneath volcanic islands [Zhong and Watts, 2013] and at subduction zones [Buffett and Becker, 2012], the evolution of friction on seismogenic faults [Boettcher, Hirth, and Evans, 2007], and subcritical crack growth in the mantle [Rice and Beltz, 1994].

Experimentally-derived equations that describe olivine plasticity are extremely variable in the stresses they predict when extrapolated to geological conditions, especially at low temperatures. Estimates of olivine strength at room temperature, for example, vary between 2 and 6 GPa (Evans and Goetze, 1979; Meade and Jeanloz, 1990; Raterron et al., 2004; Kawazoe et al., 2009; Mei et al., 2010; Druiventak et al., 2011; Faul et al., 2011; Long et al., 2011; Demouchy et al., 2013; Demouchy et al., 2014; Kranjc et al., 2016; Idrissi et al., 2016; Proietti et al., 2016), corresponding to variations in strain rate of >10 orders of magnitude. This disagreement is generally attributed to the difficulty in making these measurements at the high stresses required for practical laboratory strain rates (typically $\sim 10^{-5}s^{-1}$) to be achieved. Most minerals are brittle if deformed at these stresses, so fracture is often

suppressed by increasing the confining pressure. The technical challenges associated with apparatuses for high-pressure experiments, however, result in less reliable measurements of load and displacement than in unconfined experiments.

Furthermore, laboratory predictions of olivine strength at low temperature are in conflict with estimates of the strength of the lithosphere from geodynamic simulations and geophysical observations. For example, convection simulations that incorporate plastic yield only exhibit behavior similar to plate tectonics if the yield stress is $\sim$200 MPa (Tackley, 2000a; Tackley, 2000b; Tackley, 2000c). Similarly, observations of lithospheric flexure around Hawaii can only be reasonably modelled if the maximum stress supported by the upper mantle is $\sim$200 MPa (Zhong and Watts, 2013). In contrast, predictions of the maximum strength of the lithosphere from most previous laboratory studies are on the order of 1 GPa (Evans and Goetze, 1979; Raterron et al., 2004; Mei et al., 2010).

To improve upon previous experimental work, we examined low-temperature plasticity in olivine using nanoindentation, a technique that generates a confining pressure in the sample, allowing plastic behavior to be accessed even at room temperature. Yield stress can be calculated from indentation experiments through its relation to hardness (the ratio of applied load to the projected area of the indent) (Tabor, 1970). Early work on olivine by Evans and Goetze, 1979 used a 4-sided pyramidal (Vickers) indenter in a dead-weight microindentation system and measured the size of the residual indent to calculate hardness and yield stress. A more recent approach by Kranjc et al., 2016 used nanoindentation and a 3-sided pyramidal (Berkovich) indenter tip, which relies on a calibrated area function to determine the mechanical properties of the indented material. Due to the sharpness of the indenter tips in these types of experiments, materials yield plastically almost immediately upon application of load with little preceding elastic deformation, and the stress state beneath the tip is very complex. Therefore, while we performed some Berkovich indents to directly compare with previous olivine indentation studies (Evans and Goetze, 1979; Kranjc et al., 2016), we predominantly used spherical indenter tips to examine the plastic

behavior of olivine.

Spherical nanoindentation has several significant benefits over previously used methods. First, the elastic-plastic transition is well-defined, especially for hard materials like olivine. Second, the contact between a sphere and a flat surface is described by simple analytical solutions for the elastic stress state beneath the sphere (Johnson, 1985). The stress at the elastic-plastic transition (the yield stress) can therefore be easily determined without relying on instrument calibrations. Finally, hardness can be calculated as a function of strain for the entire test, revealing mechanical behavior comparable to that seen in stress-strain curves for large-scale tests (Pathak and Kalidindi, 2015).

3.2 Results

We performed over 800 room-temperature nanoindentation experiments on both single-crystal (Fig. 3.1) and polycrystalline olivine. Experiments in which the indenter/sample contact is not entirely elastic leave residual indents, evident in both electron micrographs (Fig. 3.1) and mechanical data. Geometrically necessary dislocation (GND) densities, measured by high angular-resolution electron backscatter diffraction (Wallis et al., 2016), are present around the residual indents (Fig. 3.1), demonstrating the activation of plastic deformation mechanisms. Cracks are also present around the indents (Fig. 3.1), but sectioning by focused ion beam suggests that they form during unloading and therefore do not affect the yielding behavior observed in the mechanical data.

Large "pop-in" events are sometimes present in indentation tests on single crystals and can be recognized as an abrupt increase in displacement followed by a large stress drop. These pop-in events occur at the elastic-plastic transition as revealed in hardness-strain curves from spherical indentation tests (Fig. 3.2), but the hardness at which the pop-in occurs is stochastic (Fig. 3.3). The observed range of hardness values at pop-in is wider for spherical indenter tips with smaller radii, and much larger hardnesses can be reached prior

to the pop-in with these tips. Notably, pop-ins are not present in tests on polycrystalline samples of olivine that have been previously deformed at high temperature (Fig. 3.2). However, the hardness after yield in the polycrystalline samples is remarkably consistent with that seen after pop-ins in single crystals.

Projection of the plastic portion of the hardness-strain curve back to the elastic portion gives an estimate of the hardness at yield (Fig. 3.2). In 150 tests performed using an indenter tip 3 μm radius across 25 crystal orientations, the average yield hardness is 12.5 $\pm$ 1.1 GPa. Although olivine is anisotropic at high temperature (Durham, Goetze, and Blake, 1977; Bai, Mackwell, and Kohlstedt, 1991), the yield hardness at room temperature depends very little on crystal orientation, varying less than 8% among orientations for the 10 single-crystal orientations tested (Fig. 3.2). This lack of anisotropy may be due in part to the nature of spherical indentation, as evidenced by our observation of reduced anisotropy associated with the elastic (Young's) modulus. The degree of elastic anisotropy measured here (variation of $\sim$30%) is reduced relative to that measured by other methods (variation of $\sim$45%) (Abramson et al., 1997), due to out-of-plane forces inherent to the geometry of a spherical indentation test (Fig. 3.2).

A major observation in our data set is that yield hardness varies as a function of indenter size. Tests with smaller indenters exhibit larger hardness values (Fig. 3.3), a phenomenon commonly referred to as a "size effect" in the materials science literature (Swadener, George, and Pharr, 2002; Pharr, Herbert, and Gao, 2010). Measuring the magnitude of this size effect in hardness is critical for understanding how length-scales of deformation can modify lithospheric strength and for properly scaling laboratory results to geological conditions. The size effect measured by spherical indentation can be characterized by a power law with an exponent of -0.12, i.e., yield hardness is proportional to a -0.12 where a is contact radius (Fig. 3.3). The maximum hardness at pop-in is also a function of contact radius (Fig. 3.3), defined by a power law with a length-scale exponent of -0.47. These two power laws define an envelope bounding the size effects in the dataset (Fig. 3.3).

The magnitude of the size effect observed by spherical indentation is similar to that observed by Berkovich indentation (Fig. 3.3). In the latter, the indented material yields almost immediately upon loading, and hardness decreases while the effective contact radius increases over the course of the test. Changes in hardness during the loading portion of the tests give a size-effect exponent of -0.08. Hardness values obtained from unloading curves in multiple tests have a similar dependence on contact radius with an exponent of -0.07. This similarity in size effects observed in spherical indentation and Berkovich indentation is especially striking considering these are two very different types of experiment with different data processing methods. The size effect observed in olivine is broadly similar to those reported in industrial ceramics (Chromik et al., 2003).

3.3 Discussion

Overall, we observe two different size effects in our data: 1) variations in the presence and maximum hardness of pop-ins (Fig. 3.2 and 3.3), and 2) variations in hardness at yield (Fig. 3.3), both as functions of the size of the indenter contact (contact radius). The presence of pop-ins in relatively pristine single crystals, and the associated lack of pop-ins in samples with grain boundaries and dislocation substructures, is consistent with observations in metals and ceramics, where pop-ins are interpreted as bursts of dislocation nucleation and motion (Shim et al., 2008). The pre-deformed polycrystalline sample has abundant dislocation sources, therefore grains in this sample yield at a stress consistent with the activation of those sources. The single crystals used here, however, have a lower initial density of dislocation sources. Therefore, some indents must proceed to greater depths and larger average stresses in order for the stressed region to be large enough to activate enough dislocation sources. These effects can be mitigated by using a larger indenter, which dramatically reduces the maximum pop-in hardness relative to the yield hardness (Fig. 3.3).

In the second size effect, the yield hardness is directly related to the volume of the plastically deformed region, even when abundant dislocation sources are present. The size effects observed in both spherical and Berkovich indentation tests on olivine are of the same order as those seen in indentation tests on ceramics (Bull, Page, and Yoffe, 1989). This "smaller is stronger" phenomenon has been previously explained as a result of the role of strain gradients and associated GNDs in modifying plastic behavior (Nix and Gao, 1998; Durst, Backes, and Göken, 2005). For the same total strain, smaller indenters create a smaller deformed region in which to store GNDs. Thus, the GND density in the plastically deforming region is likely higher for smaller indents, increasing the hardness of the material by limiting dislocation motion through both short-range and long-range interactions. The Hall-Petch effect, in which a material with a very small grain size exhibits higher flow strength than one with a larger grain size, is thought to arise from the same source (Li, Bushby, and Dunstan, 2016; Dunstan and Bushby, 2014): in smaller grains, higher strain gradients form for the same strain, and dislocations associated with these strain gradients interfere with further dislocation motion and deformation. Thus, when low-temperature plasticity is the dominant deformation mechanism, the strength of polycrystalline olivine should also increase with decreasing grain size, likely following a power law similar to that observed in indentation tests.

Size effects have not been considered in previous studies of low-temperature plasticity in olivine. However, most previous experiments were likely affected by size effects since they were either 1) conducted using indentation techniques with inherently small regions of plastic deformation or 2) conducted on polycrystalline aggregates with small grain sizes. Therefore, we suggest that size effects constitute the major source of disagreement among published results. We compare our measured size effects with flow laws from previous studies extrapolated to room temperature in Fig. 3.4, after first converting hardness values from our indentation data to yield stresses. This analysis of different flow laws reveals a similar power-law relationship between length-scale (grain size for polycrystalline

deformation and contact radius for indentation tests) and room-temperature strength as observed in our indentation tests, demonstrating that a size effect can account for most of the discrepancy in published data.

Importantly, the observed size effect in yield stress suggests that data from samples with large inherent length scales (Druiventak et al., 2011; Idrissi et al., 2016) best represent the plastic strength of olivine in the coarse-grained upper mantle (Behn, Hirth, and Elsenbeck II, 2009; Pearson, Canil, and Shirey, 2014). Thus, we suggest that the flow law from Idrissi et al., 2016 is the best available for capturing the strength of coarse-grained mantle (Fig. 3.4) and indicates that the upper mantle is weak relative to previous experimental predictions. This particular flow law is based on the incorporation of measurements of dislocation velocity into a micromechanical simulation, which does not involve any inherent size effects. Notably, it predicts a maximum strength of the lithosphere on the order of 100s of MPa, in much better agreement with geodynamic and geophysical estimates of lithospheric strength than with most published flow laws (Evans and Goetze, 1979; Raterron et al., 2004; Kawazoe et al., 2009; Mei et al., 2010; Faul et al., 2011; Long et al., 2011; Kranjc et al., 2016).

Another major geophysical implication of the size effect in olivine is that fine-grained peridotite aggregates deforming by low-temperature plasticity will be stronger than their coarse-grained equivalents. This behavior is opposite to that observed in tests on polycrystalline olivine at higher temperatures, which activate deformation mechanisms for which strength increases with increasing grain size (Pearson, Canil, and Shirey, 2014). The compilation of published olivine plasticity data in Fig. 3.4 allows us to estimate the length scale below which decreasing grain size will strengthen olivine. This critical length scale is approximately 300 μm, which is comparable to or larger than grain sizes in exhumed mylonitic mantle shear zones (Hansen, Zimmerman, and Kohlstedt, 2011; Warren and Hirth, 2006; Toy et al., 2009). In shear zones that localize strain due to grain-size reduction during deformation at high temperatures, low-temperature plasticity will be a relatively strong

mechanism. Thus, further deformation will more likely occur via other mechanisms, such as brittle fracture (e.g., pseudotachylite overprinting fine-grained shear zones in Skemer et al., 2009).

Finally, a size effect has important consequences for the deformation and evolution of olivine-rich faults in mantle rocks. Experimental rate-and-state friction tests on most geologic materials reveal a "critical slip distance," which is commonly interpreted as the average asperity size (Fig. 3.4), on the order of tens of microns (Dieterich, 1979). In addition, experiments have suggested that contact pressures on asperities are large enough to induce plastic deformation, even for harder geologic materials such as olivine (Dieterich and Kilgore, 1994). As plastic deformation of microscopic asperities on faults is akin to that which occurs in an indentation test, the size effect seen in our experiments will also exist on faults (i.e., asperity strength will increase with decreasing asperity size). For a distribution of asperity sizes, the presence of a size effect could result in intrinsic heterogeneity in the mechanical and frictional properties of faults, which may control the evolution of fault roughness. Our results are also consistent with predictions from previous work on fault roughness (Brodsky, Kirkpatrick, and Candela, 2016), which suggests a link between length-scale and strength.

Although much work remains to be done in characterizing size effects across the range of geologically relevant materials, this study demonstrates their impact on a wide range of geodynamic phenomena involving deformation of the lithosphere.

3.4 Acknowledgements

Funding: Support for this research was provided by NERC NE/M000966/1, NSF EAR-1255620, NSF EAR-1464714, and NSF EAR-1550112. DEJA acknowledges funding from the Royal Academy of Engineering through a research fellowship. Any opinions, findings, and conclusions or recommendations expressed in this material are those of the authors

and do not necessarily reflect the views of the National Science Foundation, the Natural Environment Research Council, or the Royal Academy of Engineering.

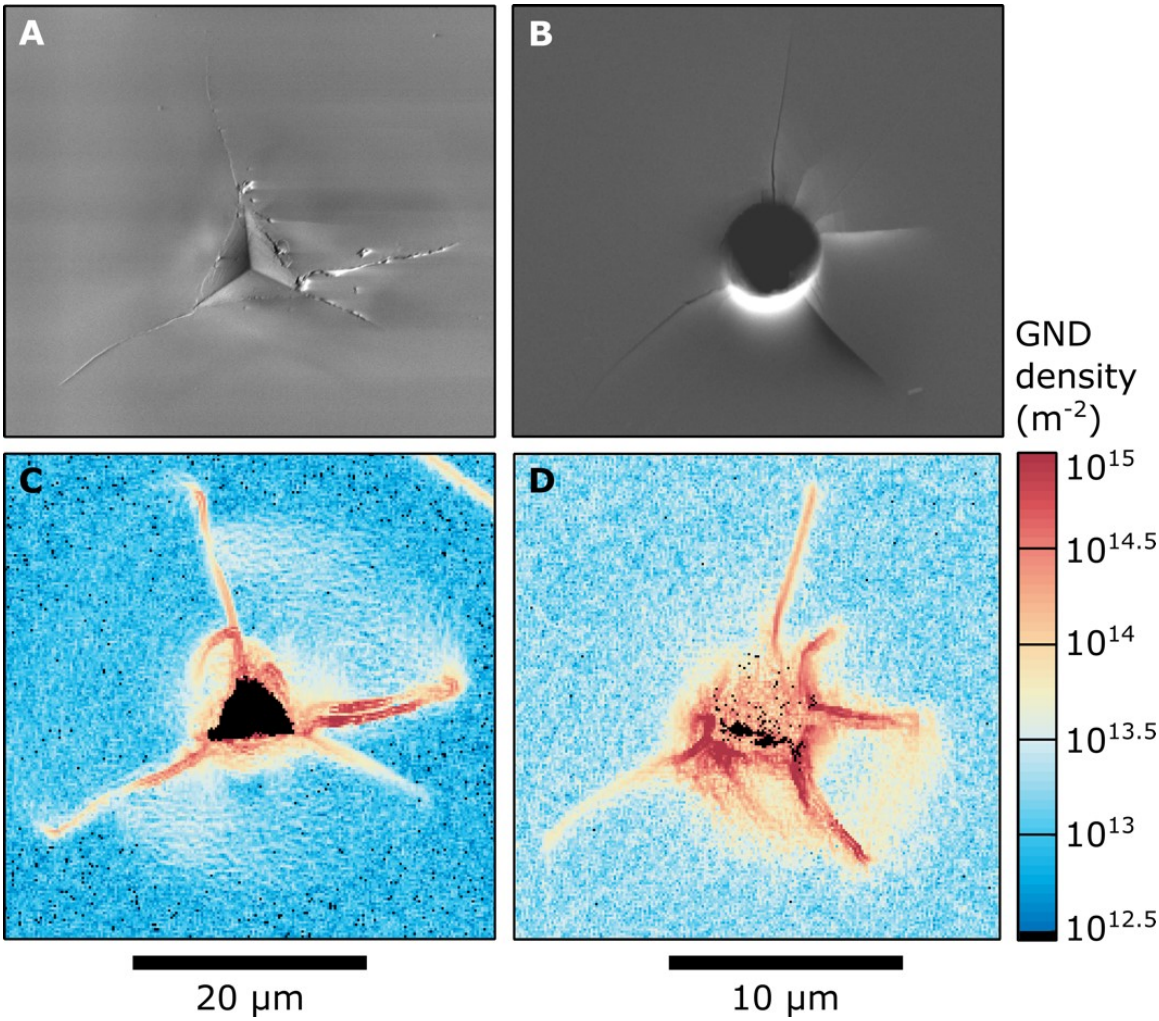

FIGURE 3.1: Examples of Berkovich and spherical indents. **(A)** Secondary electron image of a Berkovich indent. **(B)** Forescattered electron image of a spherical indent. (**C** and **D**) Maps of the GND densities associated with each indent as measured by HR-EBSD (Wallis et al., 2016). The activation of plastic deformation mechanisms is shown by the elevated densities of GNDs around the residual indents. Radial fractures emanating from the indents result in artificially high GND densities in the immediate vicinity of these cracks. Regions of each map outside the plastic zone of the indents reveal the minimum resolvable dislocation density by HR-EBSD, which varies for each map based on the analytical conditions and crystal orientation.

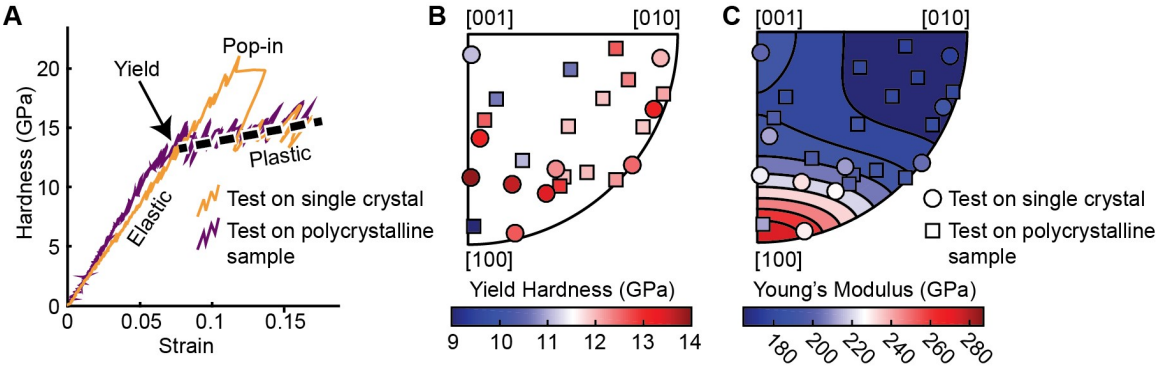

FIGURE 3.2: Summary of spherical indentation results. **(A)** Sample hardness-strain curves from tests with a 3 μm radius indenter. The dashed black line is a linear fit to the hardness data after pop-in for the single crystal. This fit is projected back to the elastic portion of the data to calculate the yield hardness. **(B)** Inverse pole figure (IPF) representing the average hardness at yield calculated for each crystal orientation tested via spherical indentation. Each marker for a single-crystal sample represents the average of 16 tests. Each marker for the polycrystalline sample represents a single indentation test on one grain of the sample. **(C)** IPF illustrating the measured Young's modulus for the same orientations as in **(B)**. The background is colored by the theoretical Young's modulus from Abramson et al., 1997.

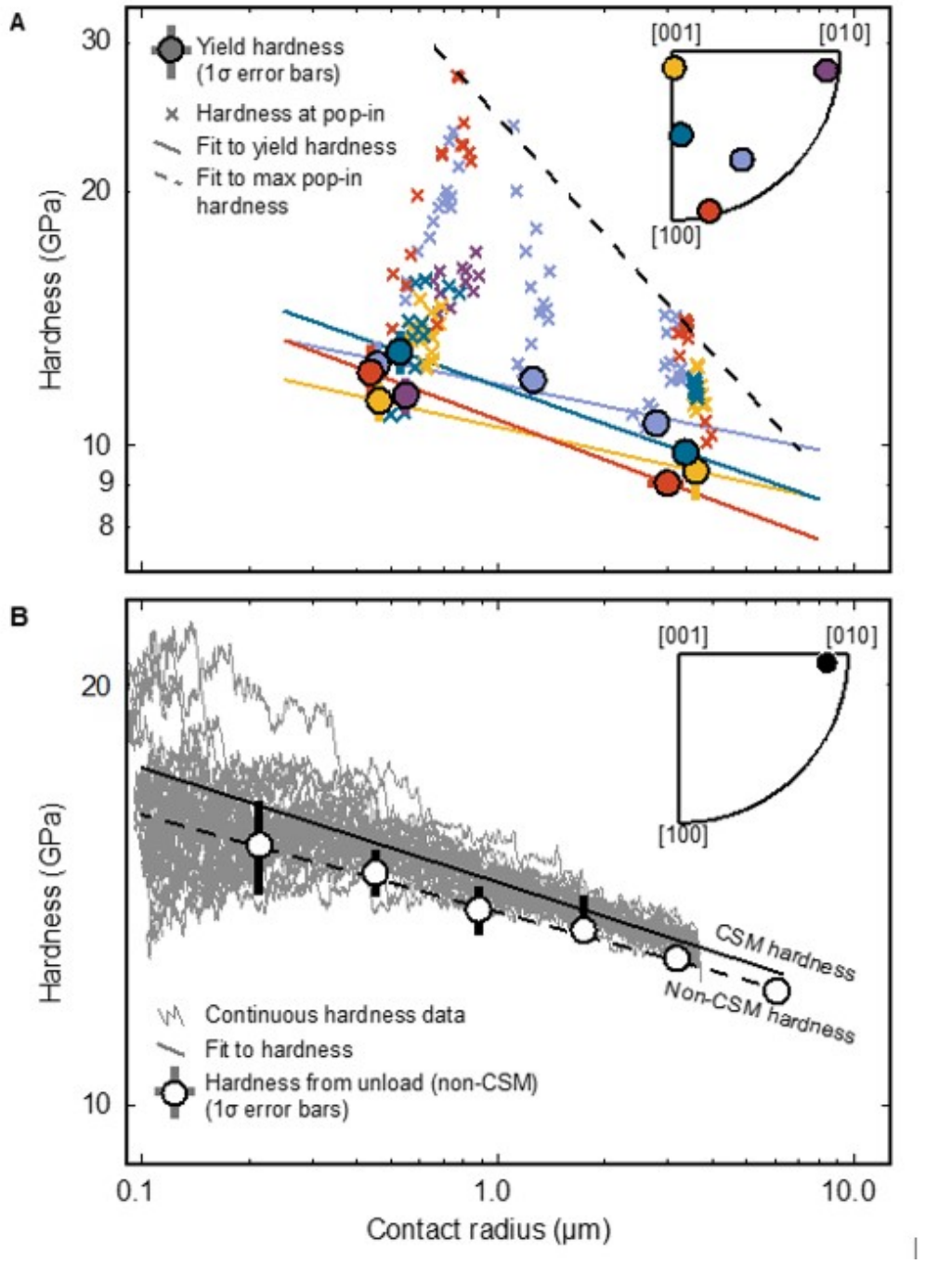

FIGURE 3.3: Size effects observed by spherical and Berkovich indentation. **(A)** Spherical indentation size effect for four different orientations of olivine as a function of contact radius at yield. Data for a fifth orientation (shown in purple) are also plotted but were only measured with a single indenter tip. Plotted values of yield hardness are averages over 12 to 16 tests. **(B)** Berkovich indentation size effect for a single orientation of olivine, as illustrated in the inset. Markers for non-CSM (continuous stiffness measurement) tests are averages of 6 to 10 tests.

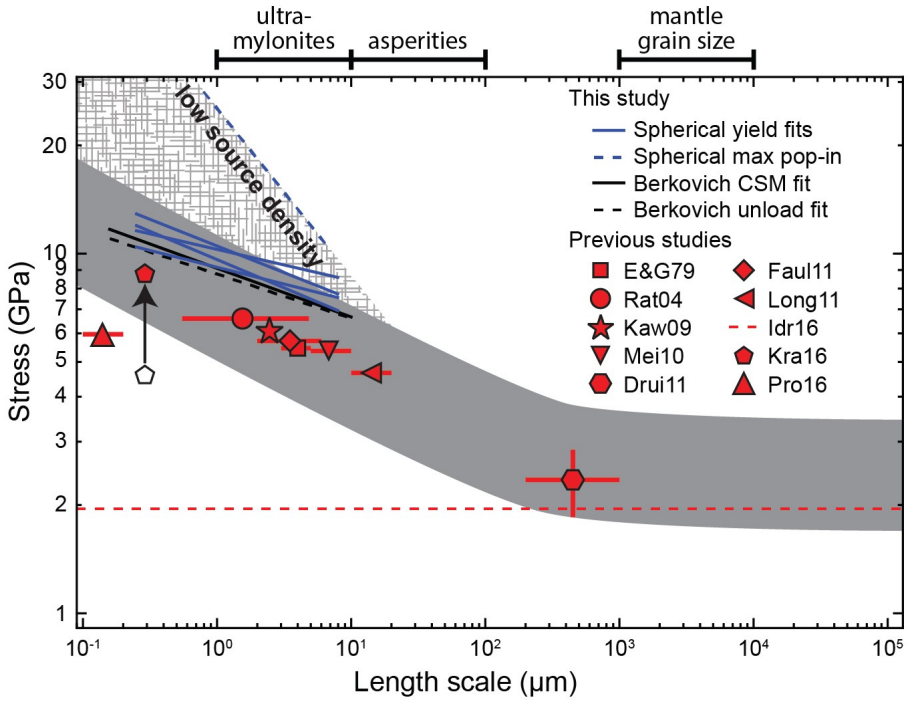

FIGURE 3.4: Comparison between observed size effects in our indentation tests and previously published low-temperature plasticity flow laws extrapolated to room temperature. Yield stresses from flow laws are calculated for a strain rate of 0.01 s^{-1} and a confining pressure of 3 GPa to approximately match the strain rate and confining pressure of indentation tests. Data from Druiventak et al., 2011 are not from a flow law but are approximate yield stresses from experiments obtained at room temperature and confining pressures of 2.0 to 2.5 GPa. These yield stresses likely reflect plasticity before any brittle deformation. Flow laws from past indentation studies (Evans and Goetze, 1979; Kranjc et al., 2016), as well as indentation data from this study, are plotted using contact radius as the length scale, whereas flow laws based on tests on polycrystalline samples (Raterron et al., 2004; Kawazoe et al., 2009; Mei et al., 2010; Druiventak et al., 2011; Faul et al., 2011; Long et al., 2011; Proietti et al., 2016) are plotted using grain size. The predicted yield stress from Idrissi et al., 2016, in which dislocation velocity was measured to calibrate a flow law, is assumed to be independent of scale. The predicted yield stress from Kranjc et al., 2016 has been rescaled following the method used by Evans and Goetze, 1979 to calculate the constraint factor (the original data point is plotted as an open pentagon). This rescaling has been performed so that all estimates from indentation experiments using sharp tips are processed in the same manner. The dark gray band represents the approximate size effect observed in all data, with the hatched gray field indicating even larger yield stresses when the dislocation source density is low. Relevant geological length scales are indicated (Behn, Hirth, and Elsenbeck II, 2009; Pearson, Canil, and Shirey, 2014; Warren and Hirth, 2006; Toy et al., 2009; Skemer et al., 2009; Dieterich, 1979; Dieterich and Kilgore, 1994). The predicted stress from Demouchy et al., 2013 is not included because their flow law is calibrated using the maximum stress observed in experiments rather than the yield stress.

Chapter 4

Constraining the Mechanism of Frictional Aging with Nanoindentation

A version of this chapter was previously published as: **Thom, C.A.**, Carpick, R.W. and Goldsby, D.L. (2018), Constraints on the physical mechanism of frictional aging from nanoindentation. *Geophysical Research Letters* **45** (24), 13,306-13,311. doi:10.1029/2018GL080561

Abstract

The increase in the frictional strength of rocks with the time of quasi-stationary contact, known as frictional aging, may ultimately determine whether unstable slip (i.e. earthquakes) can nucleate. In spite of its importance, the physical mechanism that underlies frictional aging in rocks is still uncertain. The widely held view is that aging results from an increase in contact area due to asperity creep. Here we show via nanoindentation testing that the hardness and creep rate of quartz are independent of relative humidity from < 10^{-4} to 50%. This contrasts strongly with the standard interpretation of previous friction experiments on quartz tested over a similar humidity range, which reveal an absence of frictional aging for humidity < 5%. Our results demonstrate that frictional aging in quartz

cannot result from asperity creep, and instead argue in favor of other mechanisms, including time-dependent chemical bond formation or slip-induced strengthening.

4.1 Introduction

Decades of laboratory friction experiments on rocks provide an empirical basis for rate- and state-friction laws (Marone, 1998; Scholz, 2002), which are widely adopted in earthquake nucleation models and calculations (e.g. Lapusta et al., 2000; Ampuero and Rubin, 2008; Lapusta and Liu, 2009). Despite their widespread use, however, these laws lack a physical basis; that is, the physical mechanism(s) that give rise to the observed frictional behavior is (are) unknown. One of the most fundamental observations from laboratory experiments is that friction increases linearly with the logarithm of the time of quasi-stationary contact, a phenomenon often called 'aging' (Dieterich, 1972). This behavior is thought to underlie the velocity-dependence of friction, which ultimately determines whether unstable slip – earthquakes in the case of natural faults in the Earth's crust – can nucleate (e.g. Gu et al., 1984; Dieterich, 1992). Aging is classically attributed to changes in the real area of contact with time due to creep of contacting asperities (Dieterich and Kilgore, 1994). However, direct evidence for this 'contact quantity' hypothesis for aging is still lacking for deformation-resistant materials like quartz, and recent experimental results and simulations examining frictional behavior at the single-asperity level have cast doubt on its general applicability, suggesting that chemical bond formation, or 'contact quality', can play a dominant role (Li et al., 2011; Liu and Szlufarska, 2012; Li, Liu, and Szlufarska, 2014). Recent reinterpretations of data from rock friction experiments suggest that aging may also result from interfacial slip rather than static contact (Bhattacharya, Rubin, and Beeler, 2017).

Friction experiments on quartz rocks and powders under dry conditions (i.e. $< 5\%$ relative humidity, RH) at room temperature reveal an absence of frictional aging, showing

that the presence of water is required for aging to occur (Dieterich and Conrad, 1984; Frye and Marone, 2002). The authors of these studies concluded that aging occurs due to either 1) water-assisted creep of microscopic asperities in contact on experimental fault surfaces, or 2) time-dependent chemical bonding on the frictional interface in the presence of water. Interpretation 1 is often colloquially referred to as the 'contact quantity' hypothesis, wherein aging is caused by an increase in the real area of contact due to asperity creep. Interpretation 2 is often referred to as the 'contact quality' hypothesis, wherein friction increases with the increase in the number of relatively strong siloxane (Si-O-Si) bonds across a frictional interface with time, whether or not there is an increase in contact area. While both mechanisms are plausible, and definitive evidence in favor of either mechanism occurring at macroscopic rock interfaces is lacking, an increase in the real area of contact due to asperity creep is the widely accepted mechanism of frictional aging.

Here, we use the presence or absence of water in nanoindentation tests to probe the underlying physical mechanism of frictional aging and directly test the 'contact quantity' hypothesis. The frictional behavior at interfaces depends on the mechanical properties of asperities, and indentation is a well-established method to determine the hardness (Oliver and Pharr, 1992; Oliver and Pharr, 2004), yield stress (Johnson, 1970; Evans and Goetze, 1979), and creep behavior of asperities (Goldsby et al., 2004). To mimic the deformation of microscopic asperity contacts on a frictional interface, we conducted nanoindentation experiments on a single crystal of quartz with a diamond Berkovich tip to measure its indentation hardness, which is proportional to yield strength, and the rate of indentation creep. Tests were conducted at values of RH ranging from $<10^{-4}$ to 50% to determine the effects of adsorbed water on both the hardness (yield strength) and indentation creep rate. The experiments thus directly test whether the profound differences between the aging behavior of quartz rocks in dry and humid environments cited above can be attributed to water-assisted plastic deformation and creep of frictional contacts. For the 'contact quantity' hypothesis to be correct, the hardness (a measure of plasticity) and the indentation

creep rate (a measure of asperity creep) must vary dramatically with humidity. Experiments which produce no variation in the hardness or creep rate over a large range of humidity would provide very strong evidence against the 'contact quantity' hypothesis and indicate an alternative mechanism of aging.

4.2 Methods

4.2.1 Experimental Apparatus and Humidity Control

Controlled-humidity experiments were conducted in three different instruments - an iMicro Nanoindenter housed at Nanomechanics, Inc. (NMI) in Oak Ridge, Tennessee, an identical iMicro Nanoindenter housed at the University of Pennsylvania, and the MRI (Major Research Instrumentation) Prometheus Nanoindenter housed at NMI. For experiments in the NMI-housed iMicro Nanoindenter, a humidity gauge was placed inside the instrument before sealing the chamber and allowing it to equilibrate for 12-24 hours. Three different conditions were tested: ambient laboratory air (RH 25%), humidified air (RH 50%) created by placing a salt-water solution inside the chamber, and de-humidified air (RH 2-6%) created by placing silica gel desiccant inside the chamber. Experiments in the iMicro at the University of Pennsylvania were conducted either by sealing the indenter chamber and flushing it continuously with dry nitrogen gas (RH 1%), or in ambient laboratory air (RH 20%). Tests at ambient conditions (RH 30%) in the MRI Prometheus, for which the nanoindenter is located within an SEM vacuum chamber, were conducted with the vacuum chamber open and a humidity gauge located directly next to the instrument. Experiments were also performed in vacuum in Prometheus with a chamber pressure of 3.3 x 10^{-5} millibars (residual water vapor will exist due to desorption of adsorbed water from the surfaces of the chamber walls and of the indentation apparatus contained within; the largest possible value is determined by making the extreme assumption that the measured

residual gas in the chamber is entirely composed of water vapor, which corresponds to a RH of 1.25 x 10^{-4} %).

4.2.2 Hardness Protocol and Continuous Stiffness Method

Indentation tests were conducted on an dry synthetic single crystal of quartz (MTI Corporation) 1-mm thick and 1 cm^2 in area. The normal to the plane of the sample was oriented 42° from its c-axis. Three diamond Berkovich tips (one in each instrument) were used for all experiments. The area functions (i.e. the polynomial relationship describing the projected area of the indenter tip as a function of distance from its apex) of the indenter tips were calibrated using a fused silica standard before the experiments. Hardness was defined as the load divided by the projected contact area of the indenter tip, which was determined from the indentation depth and the contact stiffness (Oliver and Pharr, 1992). The contact stiffness is obtained from the slope of the unloading curve in hardness tests, and, from contact mechanics theory, is proportional to $\sqrt{A}$, where A is the contact area. We also measured hardness continuously throughout a single experiment using the continuous stiffness method (CSM) (Li and Bhushan, 2002; Oliver and Pharr, 2004) at a nominally constant strain rate, $\dot{P}/P$, where $\dot{P}$ is the loading rate and P is the load, of 0.2 s^{-1} (e.g. Lucas and Oliver, 1999). We applied a 2-nm, 100-Hz oscillation in tip displacement and measured the amplitude of the force response and the phase lag between the displacement and force to calculate stiffness, and hence contact area.

4.2.3 Creep Protocol and Analysis

Nanoindentation creep tests were performed on the same quartz single crystal using the Berkovich tips described above. Once the surface was detected, the load was increased to a target load of either 15, 40, or 400 mN at a loading rate of 1000 mN/s and held constant for up to 1 hour. The projected contact area was determined during the first 10 s of the test from the measured indentation depth, which was assumed to be equal to the contact

depth, h_c. Each value of the projected contact area during the hold was then normalized to the contact area at the end of the step-loading phase using $\frac{A_i}{A_0} = \frac{h_{c_i}^2}{h_{c_0}^2}$, where the subscripts *0* and *i* refer to the starting value and the instantaneous value, respectively. For holds longer than 10 s, the contact stiffness (*S*) was used to determine changes in the contact area using $\frac{A_i}{A_0} = \frac{S_i^2}{S_0^2}$, where the subscripts are the same as above. For creep tests, we used a 1-mN oscillation in load and measured the responding tip displacement and phase lag to determine the contact stiffness. We assume that the value of A_0 determined at 10 s from the continuous stiffness data (the point at which the continuous stiffness measurement is turned on) is equal to the value of A_i determined from the displacement (depth) data at 10 s. All subsequent measurements of contact area are derived from the continuous stiffness measurements to avoid thermal drift of the displacement data at long hold times. Finally, a linear regression was performed on all data to determine the rate of contact area growth, $\dot{A}_{norm}$.

4.3 Results

Results of the nanoindentation hardness tests are shown in Figure 4.1. The tests were conducted in two different nanoindentation apparatus at a range of RH from 2% to 50%, as well as in vacuum (at an estimated RH of $<10^{-4}$ %), overlapping the range of humidity investigated in the quartz friction experiments cited above (Dieterich and Conrad, 1984; Frye and Marone, 2002). In total, 224 indentation tests were performed, at five different values of humidity. The continuous-stiffness method was used in the tests, which allows the hardness of a sample as a function of indentation depth to be determined in a single indentation test (Li and Bhushan, 2002; Oliver and Pharr, 2004). In all tests, values of the hardness were observed to decrease with increasing depth of the indent (i.e., with an increase in the load applied to the indenter tip), a phenomenon known as the 'indentation size effect', widely observed for many engineering materials (Pharr, Herbert, and Gao,

2010) and recently identified in geological materials (Kumamoto et al., 2017; Thom et al., 2017). However, more importantly, the measured value of the hardness at a given depth is independent of humidity within the experimental uncertainty of < 5%. Our results thus indicate that the absence of aging in the friction experiments on dry quartz cited above cannot be attributed to an increase in hardness or, equivalently, yield strength, of asperities.

Indentation creep tests were also conducted over a range of humidity from RH $\sim 10^{-4}$ to 50%. As an example, in Figure 4.2, the indentation depth vs. time and contact stiffness vs. time data from a 1-hour-long indentation creep experiment conducted at an ambient humidity of RH 25% are shown. After step-loading the sample to a given load, the load was held constant. The indenter tip continued to penetrate into the material due to creep of the sample, resulting in an increase in both the indentation depth and the contact stiffness (due to the increase in the projected contact area of the indent). Only the first ten seconds of the displacement (indentation depth) vs. time data are shown, because the displacement data are sensitive to thermal drift of the instrument at longer times. The continuous stiffness data, in contrast, are insensitive to thermal drift and are thus reliable to longer contact times. For all experiments, we normalize the instantaneous projected contact area during the hold, A_i, by the projected contact area at the end of step loading, A_0, as shown in Figure 4.3, where $\frac{A_i}{A_0}$ is plotted against time for a 3600-s hold. A linear fit to these data, the slope of which is the time rate of change of the normalized contact area, $\dot{A}_{norm}$, has a value of 0.012, similar to previously reported values from nanoindentation creep tests on quartz (Goldsby et al., 2004).

Nanoindentation creep experiments in dry environments should yield drastically different values of $\dot{A}_{norm}$ compared to tests at higher humidity if water-assisted creep is the dominant mechanism of frictional aging. In the dry case, there would be no increase in indentation depth or contact stiffness (contact area) with time (i.e., no creep). Figure 4.4 compiles the results of a total of 124 indentation creep tests at 7 different values of RH ranging from $\sim 10^{-4}$ to 50%, for 3 different loads, with each data point representing an

average of 3 to 12 tests. Three different nanoindentation apparatus, and several different methods of controlling humidity, were used to acquire the data. Vertical error bars in Figure 4.4 represent one standard deviation from the mean. At all humidity conditions, the average value of $\dot{A}_{norm}$ is nearly identical, as demonstrated in Figure 4.4. At RH < 5%, a dramatic decrease in $\dot{A}_{norm}$ is expected if asperity creep is the physical mechanism of aging, as hypothesized for the friction experiments cited above (Dieterich and Conrad, 1984; Frye and Marone, 2002), but is not observed in any of our experiments.

4.4 Discussion

Our results are inconsistent with the 'contact quantity' explanation of frictional aging, wherein changes in friction are caused by changes in the real area of contact due to plasticity and creep of frictional contacts. Our results are, however, consistent with a number of recent experimental observations and simulations aimed at understanding the physical origins of aging and the 'state variable' of rate- and state-variable friction laws (RSF). For example, simultaneous measurements of friction, acoustic wave transmission (a proxy for real area of contact), and transmitted light intensity (a more direct measurement of contact area) for a frictional interface between acrylic plastic samples suggest that although there is some correlation between contact area and friction, the correlation is not one-to-one (Nagata et al., 2014). We note that although the rate at which contact area increases in our experiments, $\sim$1% per decade, is consistent with the rate of frictional aging in rock friction experiments (for example, $\sim$2% per decade of time in experiments on quartz-rich rocks (Dieterich, 1972)), the strength of the frictional interface cannot be controlled by solely by contact area.

An alternative to the 'contact quantity' explanation of aging is that the logarithmic increase in friction with time observed in rock friction experiments (Dieterich, 1972; Marone,

1998; Scholz, 2002) is caused by changes in the chemical bonding state across the contacting interface. Time-dependent formation of siloxane (Si—O—Si) bonds between a pair of opposing hydrolyzed silica groups (Si—OH) has been shown via atomic force microscopy (AFM) to be a viable mechanism of frictional aging for nanoscale single-asperity silica-silica contacts (Li et al., 2011). Molecular simulations confirm the AFM results and shown that the number of siloxane bonds across a silica-silica interface increases linearly with the logarithm of contact time for an elastic contact (Liu and Szlufarska, 2012; Li, Liu, and Szlufarska, 2014). Thus, strong frictional aging occurs even in the absence of plastic deformation. Creep of asperities must play an indirect role in aging, by increasing the area of contact over which chemical bonding can occur, but our results suggest that the formation of chemical bonds at contact junctions, or another unknown mechanism, is the primary physical mechanism that gives rise to aging. Our results also indirectly support recent reinterpretations of data from rock friction experiments that highlight the possible importance of slip rather than contact time in frictional aging. Therefore, the physical origins of aging, and the associated state variable in rate- and state-variable friction laws, must be reevaluated.

4.5 Conclusions

We have performed hardness and nanoindentation creep experiments on a single crystal of quartz to determine if plasticity or creep are affected by relative humidity. Over the range of humidity tested, there is no difference in either the hardness or indentation creep behavior of quartz. These results are inconsistent with predictions of the 'contact quantity' hypothesis for frictional aging, suggesting that changes in contact area alone cannot explain frictional aging. Some other mechanism, such as time-dependent chemical bonding or slip-induced strengthening of asperities must control frictional aging of quartz rocks.

4.6 Acknowledgements

The authors would like to thank G. Pharr, W. Oliver, and K. Johanns for assistance in performing the experiments and T. Tullis for discussions. This research was supported by the National Science Foundation through awards EAR 1464714 and EAR 1550112. The authors declare no competing interests. All data presented in this study is available at `https://upenn.box.com/s/rrgamthcpgn5lqkvyp6s7slhj6zuw87i`.

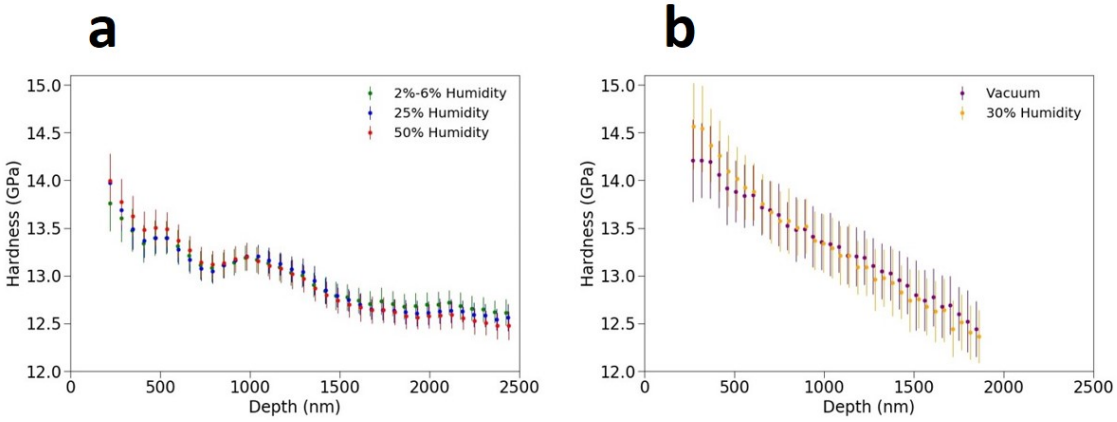

FIGURE 4.1: Nanoindentation hardness at several relative humidity conditions. Data from tests in **(a)** an iMicro Nanoindenter (1-atm apparatus, Nanomechanics, Inc.) and **(b)** the MRI Prometheus Nanoindenter (high-vacuum apparatus, Nanomechanics, Inc.) show no difference in hardness at any humidity over the full indentation depth range investigated in each instrument. For tests yielding the data in **(b)**, the RH 30% data were obtained with the vacuum chamber open to room atmosphere. Error bars in **(a)** and **(b)** represent one standard deviation from the mean. Data in **(a)** and **(b)** may not be directly comparable due to differences in tip orientation relative to the crystallographic orientation of the sample in each nanoindenter.

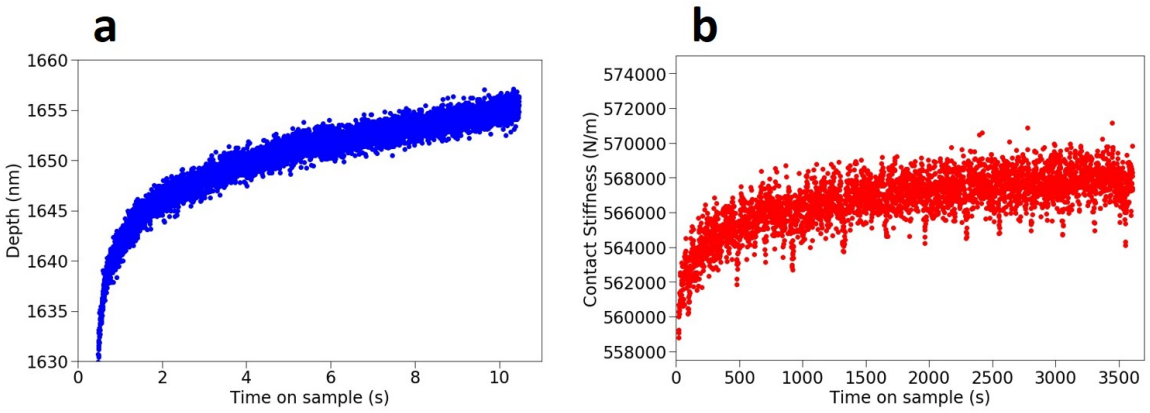

FIGURE 4.2: Typical results for a 3600-s nanoindentation creep test at RH = 25%. During the first portion of the test (not shown), the indenter tip penetrates into the sample as it is loaded to a peak load of 400 mN. After this initial loading phase, the load is held constant, and the tip continues to penetrate more slowly with time due to specimen creep, resulting in an increase in both **(a)** the measured depth and **(b)** the contact stiffness, with time.

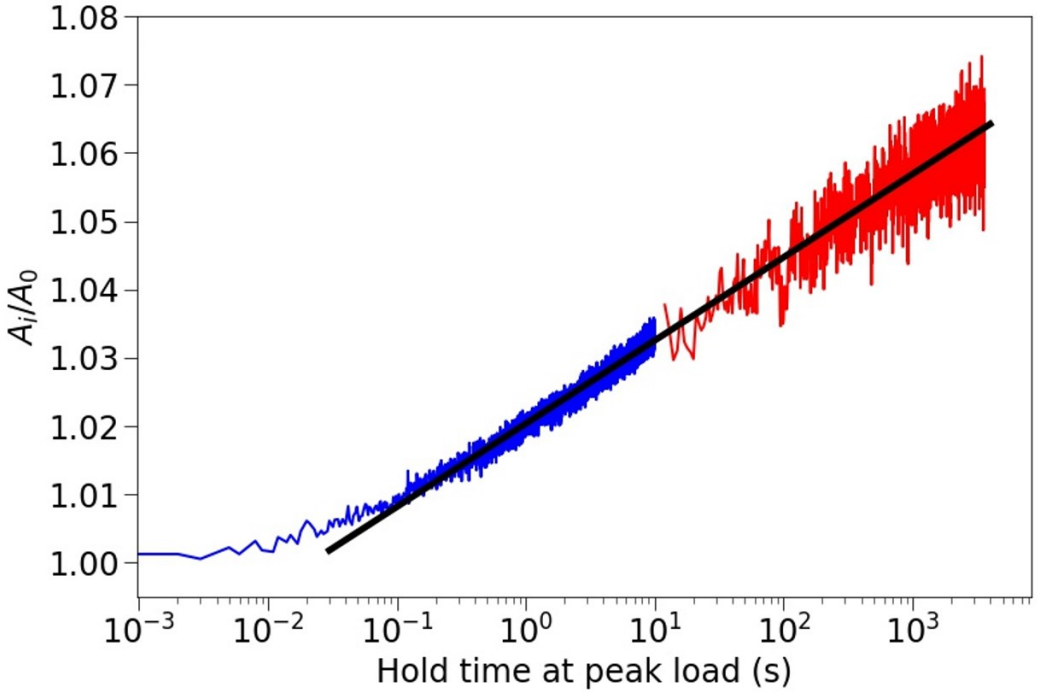

FIGURE 4.3: Normalized projected contact area $\frac{A_i}{A_0}$ as a function of the logarithm of hold time at RH = 25%. The normalized contact area derived from the depth data for the first ten seconds of the test is shown in blue. The normalized contact area derived from continuous stiffness data is shown in red for the remainder of the 3600-s hold. The black line is a best-fit line to all the data, with a slope equal to $\dot{A}_{norm}$, the rate of change of the normalized contact area with time. The slope of the black line in this example is 0.012.

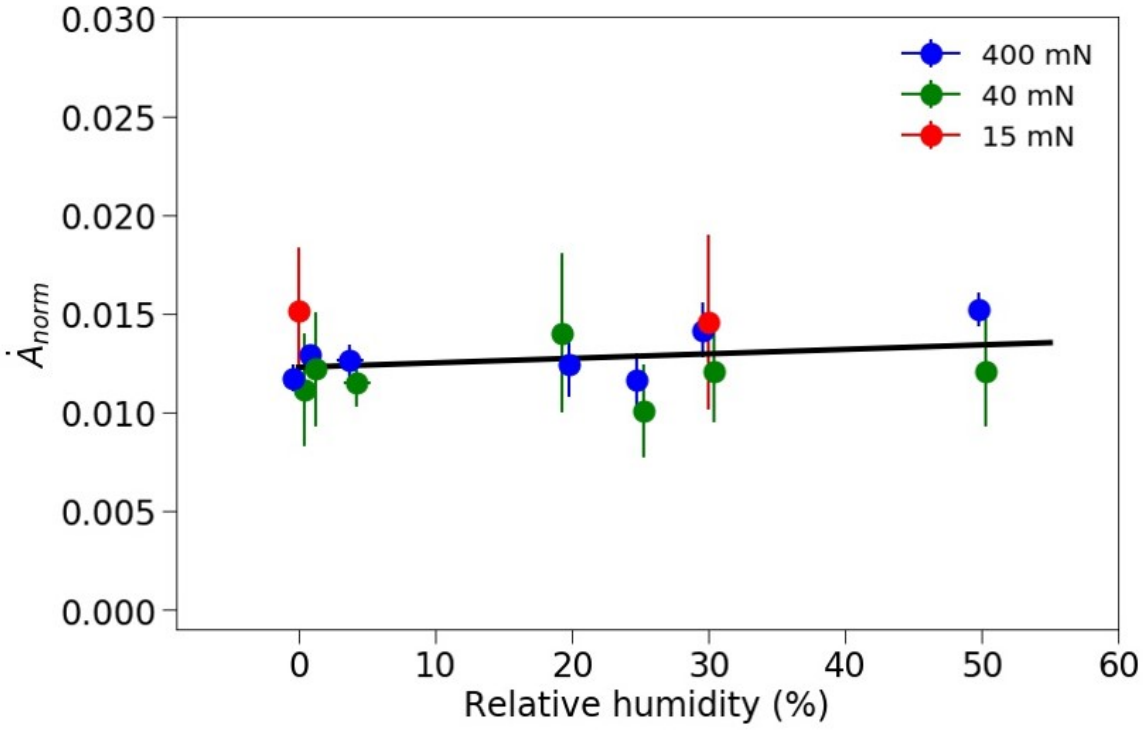

FIGURE 4.4: Rate of change of the normalized projected contact area, $\dot{A}_{norm}$, as a function of relative humidity. Each data point represents an average of 3 to 12 tests at a given load (represented by the color) and humidity, and error bars represent one standard deviation from the mean. A best-fit line is shown in black, demonstrating no dependence of the rate of normalized contact area growth on humidity. If aging were caused by contact area growth, experiments for RH < 5% would show $\dot{A}_{norm}$ dramatically falling towards zero, which is strongly inconsistent with our experimental results.

Chapter 5

Nanoindentation Studies of Plasticity and Dislocation Creep in Halite

A version of this chapter was previously published as: **Thom, C.A.** and Goldsby, D.L. (2019), Nanoindentation studies of plasticity and dislocation creep in halite. *Geosciences* **9** (2), 79. doi: 10.3390/geosciences9020079

Abstract

Previous deformation experiments on halite have collectively explored different creep mechanisms, including dislocation creep and pressure solution. Here, we use an alternative to conventional uniaxial or triaxial deformation experiments - nanoindentation tests - to measure the hardness and creep behavior of single crystals of halite at room temperature. The hardness tests reveal two key phenomena: 1) strain rate-dependent hardness characterized by a value of the stress exponent of $\sim$25, and 2) an indentation size effect, whereby hardness increases with decreasing size of the indents. Indentation creep tests were performed for hold times ranging from 3600 to 10^6 s, with a constant load of 100 mN. For hold times longer than 3 x 10^4 s, a transition from plasticity to power-law creep is observed as the stress decreases during the hold, with the latter characterized by a value of the stress exponent of 4.87 $\pm$ 0.91. An existing theoretical analysis allows us to directly

compare our indentation creep data with dislocation creep flow laws for halite derived from triaxial experiments on polycrystalline samples. Using this analysis, we show an excellent agreement between our data and the flow laws, with the strain rate at a given stress varying by less than 5% for a commonly used flow law. Our results underscore the utility of using nanoindentation as an alternative to more conventional methods to measure the creep behavior of geological materials.

5.1 Introduction

Quantifying the deformation rate of halite has been an active area of study for several decades, due largely to interest in nuclear waste storage and hydrocarbon exploration. While the goal of many authors has been to understand the large-scale behavior of salt bodies in the Earth (Jackson and Talbot, 1986; Van Keken et al., 1993; Li et al., 2012), others have aimed at understanding the fundamental microphysical mechanisms that give rise to creep, plasticity, and frictional sliding of halite (Heard, 1972; Heard and Ryerson, 1986; Wawersik and Zeuch, 1986; Carter et al., 1993; Franssen, 1994; Hunsche and Hampel, 1999; Ter Heege, De Bresser, and Spiers, 2005; Schoenherr et al., 2007; Linckens, Zulauf, and Hammer, 2016; Carter and Hansen, 1983; Skrotzki and Liu, 1982; Skrotzki and Haasen, 1988; Senseny et al., 1992; Berest and Brouard, 1998; Fossum and Fredrich, 2002; Spiers et al., 1986; Urai et al., 1986; Spiers, Urai, and Lister, 1988; Spiers et al., 1990; Urai and Spiers, 2007; Shimamoto, 1986; Shimamoto and Logan, 1986; Chester, 1988). The development of flow laws for various creep mechanisms in halite, and characterization of their associated microstructures, allows for reliable extrapolation of laboratory-derived behavior to natural conditions.

Many studies have explored dislocation creep in polycrystalline halite (Heard, 1972; Heard and Ryerson, 1986; Wawersik and Zeuch, 1986; Carter et al., 1993; Franssen, 1994; Hunsche and Hampel, 1999; Ter Heege, De Bresser, and Spiers, 2005; Schoenherr et al.,

2007; Linckens, Zulauf, and Hammer, 2016). The rate-limiting process in the dislocation creep regime, up to temperatures of 200°C, is believed to be either dislocation climb (Heard, 1972; Heard and Ryerson, 1986; Carter and Hansen, 1983) or cross-slip of screw dislocations (Wawersik and Zeuch, 1986; Ter Heege, De Bresser, and Spiers, 2005; Skrotzki and Liu, 1982; Skrotzki and Haasen, 1988; Senseny et al., 1992), but definitive evidence has not been obtained for either mechanism (Van Keken et al., 1993; Ter Heege, De Bresser, and Spiers, 2005). The dislocation creep rate can be described by an equation of the form

$$\dot{\epsilon} = A\sigma^n exp\left(\frac{-Q}{RT}\right) \tag{5.1}$$

where $\dot{\epsilon}$ is the strain rate, A is a constant, σ is the differential stress, n is the stress exponent, Q the activation energy, R the gas constant, and T the absolute temperature. Dislocation creep in polycrystalline halite is characterized by n = 5-7 (typically $n \approx 5$) and Q = 50 to 130 kJ/mol (typically Q is in the range of 50-70 kJ/mol) (Heard, 1972; Heard and Ryerson, 1986; Wawersik and Zeuch, 1986; Carter et al., 1993; Franssen, 1994; Hunsche and Hampel, 1999; Ter Heege, De Bresser, and Spiers, 2005; Schoenherr et al., 2007; Linckens, Zulauf, and Hammer, 2016; Berest and Brouard, 1998; Fossum and Fredrich, 2002). Dislocation creep experiments have been typically conducted at elevated temperatures in the range of 60-400°C and confining pressures up to 200 MPa to avoid fracturing the samples.

Although dislocation creep has been studied extensively, it is not the only mechanism by which halite can deform in the laboratory or in nature. Several studies have investigated pressure solution in the laboratory and argued that it is the dominant creep mechanism at natural geologic conditions (Spiers et al., 1986; Urai et al., 1986; Spiers, Urai, and Lister, 1988; Spiers et al., 1990; Urai and Spiers, 2007). Pressure-solution creep is grain size-sensitive, and can be described by a flow law of the form

$$\dot{\epsilon} = \frac{A\sigma^n}{d^p} exp\left(\frac{-Q}{RT}\right) \tag{5.2}$$

where d is grain size and p is the grain size exponent, equal to 3. All other parameters in Eq. 5.2 are the same as defined previously, but with different parameter values corresponding to the pressure solution mechanism. Pressure solution is observed experimentally at relatively low stresses and elevated temperatures with a characteristic value of $n = 1$. Pressure solution may dominate the deformation of halite in nature when fluids are present at low stresses and elevated temperatures.

At relatively large differential stresses, plasticity becomes the dominant deformation mechanism. A number of studies have investigated the transition from ductile deformation of halite at low shearing velocities to frictional sliding at higher slip speeds (Shimamoto, 1986; Shimamoto and Logan, 1986; Chester, 1988). At low shearing velocities, Shimamoto, 1986 reported a stress exponent of approximately 17, a value indicative of deformation limited by dislocatio glide.

Most studies of creep and plasticity of halite have employed uniaxial or triaxial apparatuses to deform macroscopic samples. While the data from such experiments are relatively simple to interpret, significant effort is required to prepare relatively large samples with uniform microstructures, maintain high temperature and high confining pressure to suppress fracture of the sample, and apply the large differential stresses and high strain rates required to measure plasticity. In this study, we explored the rheological behavior of halite at room temperature using nanoindentation. As demonstrated below, the relatively easy-to-perform indentation experiments yield data for halite that are comparable to those obtained using more conventional apparatuses.

5.2 Methods

To measure the hardness and creep behavior of halite single crystals, we performed a variety of nanoindentation tests at low relative humidity (< 15%). Although not often used

to study geological materials, nanoindentation is a well-established technique in engineering and materials science for measuring the hardness of metals and ceramics (Oliver and Pharr, 1992; Oliver and Pharr, 2004). Several indenter geometries are commonly used; we employed two different diamond Berkovich (three-sided pyramidal) indenter tips to measure indentation hardness, which is proportional to the yield stress (Johnson, 1970; Evans and Goetze, 1979; Thom et al., 2017; Kumamoto et al., 2017). By measuring the maximum applied load P_{max}, the maximum indentation depth h_{max}, and the contact stiffness S from the unloading curve, the contact depth h_c can be determined using the Oliver-Pharr method (Oliver and Pharr, 1992; Oliver and Pharr, 2004)

$$h_c = h_{max} - \epsilon_b \frac{P_{max}}{S} \tag{5.3}$$

where ϵ_b is a constant associated with the geometry of the indenter (equal to 0.75 for a Berkovich indenter). The projected contact area A_c of the indenter is a function of h_c, which is calibrated using a fused silica standard prior to the experiments. The hardness H is defined as the maximum applied load divided by the projected contact area of the indenter

$$H = \frac{P_{max}}{A_c} \tag{5.4}$$

We can also derive the effective Young's modulus of the tip-sample contact (E_{eff}) from

$$E_{eff} = \frac{\sqrt{\pi} S}{2\beta\sqrt{A_c}} \tag{5.5}$$

where β is a constant with a value close to unity. To determine the Young's modulus E_s of the sample, we employ the relation

$$\frac{1}{E_{eff}} = \frac{1-\nu_s^2}{E_s} + \frac{1-\nu_i^2}{E_i} \tag{5.6}$$

where ν is Poisson's ratio and the subscripts s and i refer to the sample and indenter, respectively. Thus, we can determine the Young's modulus of the sample using the known elastic constants of the diamond indenter and an assumed Poisson's ratio of 0.25 for the sample.

The Oliver-Pharr method described above produces only one measurement of the hardness and elastic modulus per test, which is determined from the slope of the unloading curve at peak load, at the maximum contact depth. Thus, measuring the depth-dependent hardness and modulus of the material requires numerous experiments or additional testing techniques. Using the so-called continuous stiffness method (CSM), we determined the hardness and modulus continuously at all depths in a single indent (Oliver and Pharr, 2004; Li and Bhushan, 2002). For hardness tests using the CSM, we apply a 100-Hz sinusoidal oscillation of the tip displacement (with a typical amplitude of 2 nm) and measure the resulting sinusoidal force response, and the phase lag between displacement and force, allowing the contact stiffness, and thus the contact area, hardness, and elastic modulus, to be determined continuously throughout a single test. In our nanoindentation creep tests, we used the CSM to impose a constant sinusoidal oscillation of the load of typically 2 mN about a nominally constant applied load of 100 mN and measured the resulting displacement and phase lag. Using the CSM, the contact stiffness is determined over time scales (< 0.01 s) too small for significant thermal drift to occur, allowing long-duration creep tests (up to 10^6 s in this study) to be conducted.

We performed nanoindentation hardness tests by loading the sample at constant $\frac{\dot{P}}{P}$ where P is the applied load and $\dot{P}$ its time derivative. Several different values of $\frac{\dot{P}}{P}$ were used in this study to determine the effect of loading rate and strain rate on the measured hardness.

For both the hardness and creep tests, we define the indentation strain rate $\dot{\epsilon}_i$ as

$$\dot{\epsilon}_i = \frac{1}{h_c}\frac{dh_c}{dt} \tag{5.7}$$

where $\frac{dh_c}{dt}$ is the time-derivative of the contact depth. For the hardness tests and the initial stages of creep tests, the strain rate can be calculated directly from the measured contact depth using Eq. 5.3. However, for longer hold times, thermal drift of the instrument is problematic, and h_c must be determined in a different manner. Using the known modulus of the sample measured in the hardness experiments, we can rearrange Eq. 5.5 to solve for the contact area as a function of stiffness.

$$A_c = \frac{\pi S^2}{4\beta^2 E_{eff}^2} \tag{5.8}$$

For these experiments, we use an area function of the form

$$A_c = C_1 h_c^2 + C_2 h_c + C_3 h_c^{\frac{1}{2}} + ... + C_7 h_c^{\frac{1}{32}} \tag{5.9}$$

where $C_1, C_2, C_3 ... C_7$ are constants determined from calibrations obtained from indentations on fused silica. This method allows us to directly determine the contact depth, h_c, and therefore the strain rate, from the continuous stiffness measurements made during long-duration creep tests.

We also determine the stress applied to the sample during the hold using a similar method. The hardness (stress) on the sample is the applied load divided by the projected contact area of the indenter tip. Thus, we also determine the stress using the contact area calculated from Eq. 5.8

5.3 Results

5.3.1 Constant Strain Rate Experiments

Constant strain rate tests were performed at a range of strain rates varying over two orders of magnitude. Fig. 5.1 shows the load-depth curves for a total of 116 nanoindentation

hardness tests performed at 6 different target values of $\frac{\dot{P}}{P}$. Six distinct clusters, each shown by a different color, reflect the results obtained at different target strain rates. The hardness as a function of depth is shown in Fig. 5.2 for all the tests, color-coded by the target strain rate. A significant indentation size effect is observed for all experiments, wherein the measured hardness increases with the decreasing size of the indents. This is a well-established phenomenon in engineering materials (Pharr, Herbert, and Gao, 2010), and has been observed for a number of geologic materials (Thom et al., 2017; Kumamoto et al., 2017; Thom, Carpick, and Goldsby, 2018; Chapter 2; Appendix 3). We determined the hardness at a depth of 4000 nm, at which all tests reached a steady-state strain rate, and the indents are deep enough that the indentation-size effect is negligible. In Fig. 5.3, we plot the average indentation hardness at a given strain rate at depth of 4000 nm against the steady-state indentation strain rate. The data clearly show a strain-rate dependence of the hardness, similar to materials such as indium and selenium (Lucas and Oliver, 1999; Su et al., 2013), with a stress exponent of $\sim$25.

5.3.2 Constant Load and Hold Creep Experiments

Examples of contact depth vs. time and contact stiffness vs. time data for a 3600-s hold are shown in Figs. 5.4 and 5.5. In Fig. 5.4, thermal drift of the tip displacement is noticeable at long hold times, where the apparent depth increases roughly linearly with time. However, the continuous stiffness data shown in Fig. 5.5, for which thermal drift is negligible, demonstrates that the creep rate decreases continuously during the test. Typical hardness vs. strain rate data from a constant load and hold (CLH) test with a peak load of 100 mN and a loading rate of 100 mN/s are shown in Fig. 5.6. During the initial part of the test, stress and strain rate are derived using the Oliver-Pharr method and Eq. 5.7, respectively (shown in blue). At longer times (typically beyond $\sim$10-15 s), we turn on the tip oscillation to determine the stress and strain rate for the remainder of the test using the CSM (data

shown in red). At the point where the tip oscillation is turned on, we assume that the hardness of the sample determined from both methods is identical. Only minor adjustments (< 1%) to the measured effective modulus are needed to match the two data sets at that point, using Eq. 5.8.

5.3.3 Effect of Loading Rate

We performed 20 CLH creep tests to specifically determine the effect of loading rate on deformation. Four tests each were conducted at 5 different loading rates, for hold times of one hour, the results of which are shown in Fig. 5.7. In Fig. 5.7, we only show the data derived from the displacement data obtained during the initial stages of the test, because all the tests showed the same behavior during the hour-long hold. During initial loading, data from all tests appear to be qualitatively and quantitatively similar over the range of loading rates. Tests with a larger loading rate yield initially higher values of both hardness and strain rate, but data acquired later in the tests overlap with data from tests conducted at slower loading rates. Thus, there does not appear to be a significant effect of loading rate on hardness and strain rate in the CLH tests.

5.3.4 Effect of Peak Load

We also performed 16 CLH creep tests to determine if there is an effect of peak load on deformation. We did not conduct tests at very small loads, due to the known presence of an indentation size effect, as demonstrated in Fig. 5.2. However, we performed tests at larger loads to explore other potential effects. Our results are shown in Fig. 5.8, which demonstrates that there is no effect of peak load on creep behavior over the range tested. All CLH creep tests yield data in quantitative agreement with each other during the hour-long hold.

5.3.5 Very Long Hold Creep Tests

In addition to the 1-hr CLH creep tests, we also performed 2 creep tests of much longer duration, up to 10^6 s. In these very-long hold tests, the data from the first $\sim$3 x 10^4 s of the tests were quantitatively similar to data from experiments for hold times of 1 hour. However, for longer hold times, creep appears to periodically accelerate during the test, as demonstrated by the contact stiffness data in Fig. 5.9. After each creep acceleration, long periods of time with a reduced creep rate are observed. This unsteady creep behavior is not seen in our other CLH creep tests, nor has it been reported for any material in the literature to the best of our knowledge.

We fit the contact stiffness vs. log time data as shown in Fig. 5.10. Two straight lines can be fit to the data, as shown in the figure. In Fig. 5.11, we plot the stresses and strain rates derived from the contact stiffness data from the very-long hold tests. Clearly, there is a change in the stress exponent at a hardness (stress) of $\sim$180 MPa. At high stresses, a best-fit to the data yields a value of the stress exponent similar to that obtained in the other experiments, $\sim$25, but the data at lower stress yield a value of the stress exponent of 4.87 $\pm$ 0.91, suggesting a change in the dominant deformation mechanism from plasticity to power-law creep, the latter with a typical value of $n \approx 5$ for halite.

5.4 Discussion

Compared to a uniaxial or triaxial deformation experiment, the stress state in the sample beneath a Berkovich indenter tip is complex, without any analytical solutions for the stress field. Therefore, it is not straightforward to compare data collected from macroscopic samples tested in a uniaxial or triaxial testing geometry to data acquired in nanoindentation tests. Additionally, comparing the deformation induced by an indenter in a single crystal to deformation of a polycrystalline sample is also not straightforward. However, due

to the complex stress state under an indenter, multiple slip systems must be activated, approximating the deformation of a polycrystalline aggregate (Evans and Goetze, 1979).

Recently, efforts have been made to understand and compare the creep parameters that result from nanoindentation testing with parameters derived from more conventional experiments (Su et al., 2013; Ginder, Nix, and Pharr, 2018). A theoretical treatment of the problem by Bower et al., 1993 has recently been applied to a few materials. For a full description of the analysis and a review of direct comparisons between data from macroscopic tests and nanoindentation tests, see Ginder, Nix, and Pharr, 2018. Here, we summarize a few major points. For a power-law creeping material in a nanoindentation test, the relationship between the indentation strain rate ($\dot{\epsilon_i}$) and hardness (H) can be written as

$$\dot{\epsilon_i} = \beta_i H^m \tag{5.10}$$

where β_i is a constant that captures the Arrhenius dependence of the creep rate and a material parameter akin to A in Eq. 5.1, and m is the stress exponent measured in the nanoindentation creep test. A similar form can be written for conventional compression tests. By simplifying Eq. 5.1, we can write

$$\dot{\epsilon} = \alpha \sigma^n \tag{5.11}$$

where α encompasses all of the terms besides the stress σ and the stress exponent n in Eq. 5.1. Bower et al., 1993 show that m and n are equal to each other, so the conversion between conventional and nanoindentation creep parameters is entirely captured by the functional relationship between the pre-factors β_i and α. Two quantities are needed to determine this conversion, the "pile up-sink in parameter" (c) and the "reduced contact pressure" (F). Values of these parameters are strongly dependent on the value of the stress exponent and the geometry of the indenter tip (Su et al., 2013; Ginder, Nix, and Pharr, 2018; Bower et al.,

1993). To directly convert between β_i and α, we use the relationship

$$\alpha = \frac{\beta_i F^n c^{2n-1}}{tan(\theta)} \tag{5.12}$$

where θ is the angle of the conical indenter tip and all other parameters are described above (Ginder, Nix, and Pharr, 2018). For this analysis, we treat the Berkovich tip as a cone with an angle of 70 degrees, allowing us to use finite element results from Su et al., 2013 to determine the values of *F* and *c*. Using the measured stress exponent, *n*, and the value of β_i determined from the nanoindentation data, we directly convert nanoindentation creep data to equivalent conventional creep data. As the stress exponent becomes larger, the conversion factor between the stress in conventional creep and nanoindentation creep approaches a limiting value of 3, similar to the constraint factor described by Johnson, 1970. For our data where n = 4.87, the conversion factor for stress has a value of 2.86. Alternatively, we can adjust the strain rate at a fixed stress. In this case, the nanoindentation creep rate must be multiplied by a factor of $\sim$146. Both of these conversions are shown in Fig. 5.12, where we plot both the original nanoindentation creep data and the "Bower-shifted" data. Also shown in Fig. 5.12 is the extrapolation of three different dislocation creep flow laws commonly used for polycrystalline halite. Remarkably, our Bower-shifted indentation creep data show very close quantitative agreement with the flow laws derived from "macroscopic" experiments, suggesting that our nanoindentation creep tests interrogate the same creep mechanisms as conventional creep tests performed at modestly elevated temperature and elevated confining pressure. In fact, for a given stress, our converted strain rates are within 5% of the value predicted from the Wawersik and Zeuch, 1986 flow law.

5.5 Conclusions

We have performed an extensive set of nanoindentation hardness and nanoindentation creep experiments to determine the high-stress, room-temperature rheological behavior of single crystals of halite. Our results demonstrate that the hardness of halite is sensitive to strain rate, with a stress exponent of $\sim$25 at hardness (stress) values larger than $\sim$190 MPa. We also observe a significant indentation size effect, whereby hardness increases with decreasing size of the indents. The measured rheological behavior is independent of loading rate and peak load over the range of test conditions. Nanoindentation creep tests corroborate the hardness-derived data, and reveal a distinct change in the dominant deformation mechanism with decreasing stress. We interpret this transition to n = 4.87 behavior at lower stresses as a transition from plasticity to dislocation creep, the latter typically characterized by a value of $n \approx 5$. Accounting for differences in the stress state in nanoindentation tests compared to conventional tests, we demonstrate that our nanoindentation data are in excellent agreement with flow laws for dislocation creep of halite derived from triaxial tests on polycrystalline samples. Our results underscore the utility of using nanoindentation in addition to more conventional methods to measure the creep behavior of geological materials at ambient and, in the future, elevated temperatures.

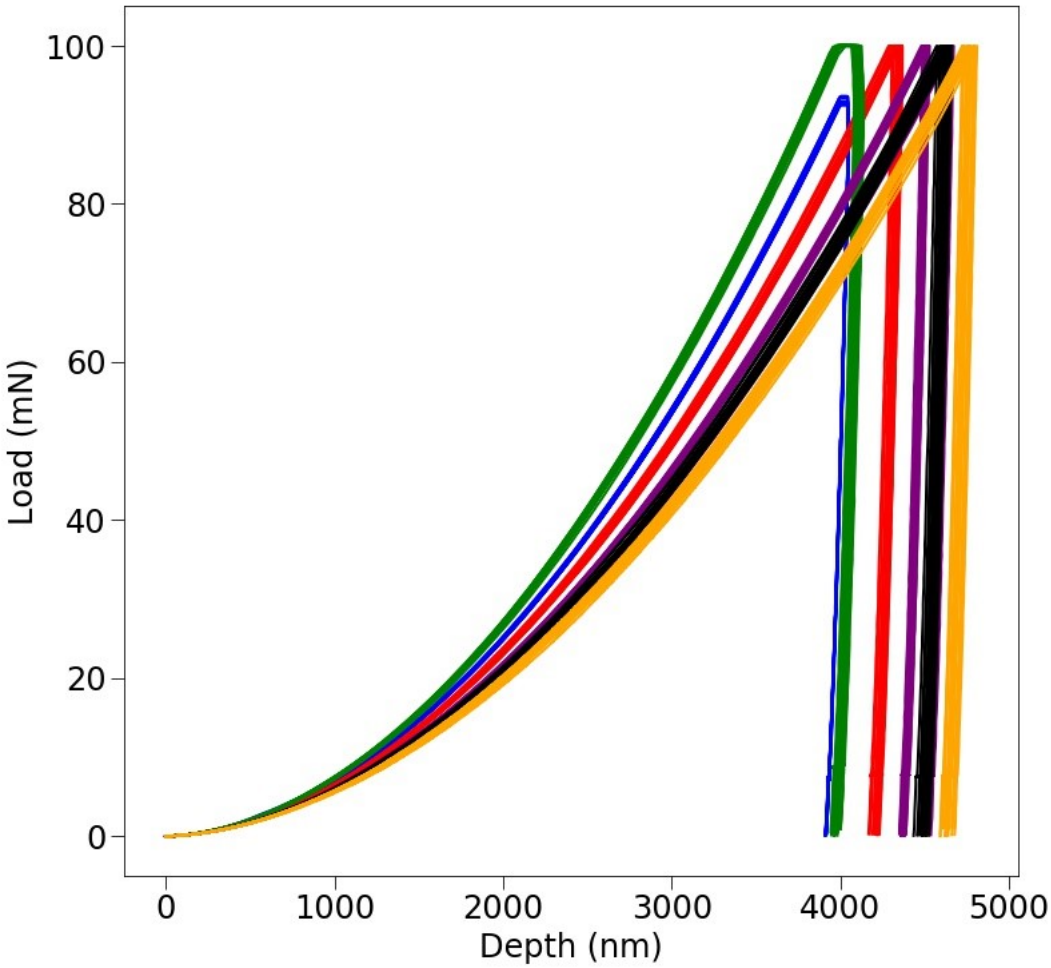

FIGURE 5.1: Load vs. depth curves for all 116 nanoindentation hardness tests performed on halite. Each color represents ∼20 tests at target strain rates of 0.40 (green), 0.14 (blue), 0.05 (red), 0.015 (purple), 0.0075 (black), and 0.0015 (orange). The nearly vertical unloading portion of the data indicates that plasticity dominates the deformation, and that very little elastic recovery occurs at the end of the test.

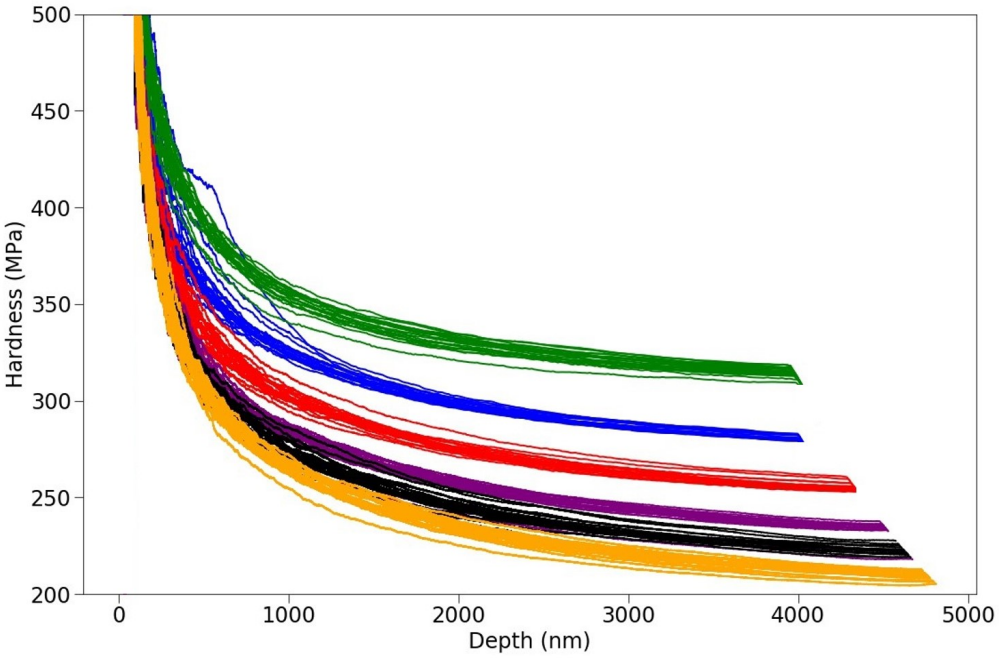

FIGURE 5.2: Plot of indentation hardness as a function of depth. At shallow indentation depths (< 1000 nm), a significant size effect can be observed, whereby hardness increases dramatically with decreasing indentation depth, for all target strain rates. At larger indentation depths, the size effect is small, and the hardness approaches a steady-state value corresponding to the given target strain rate.

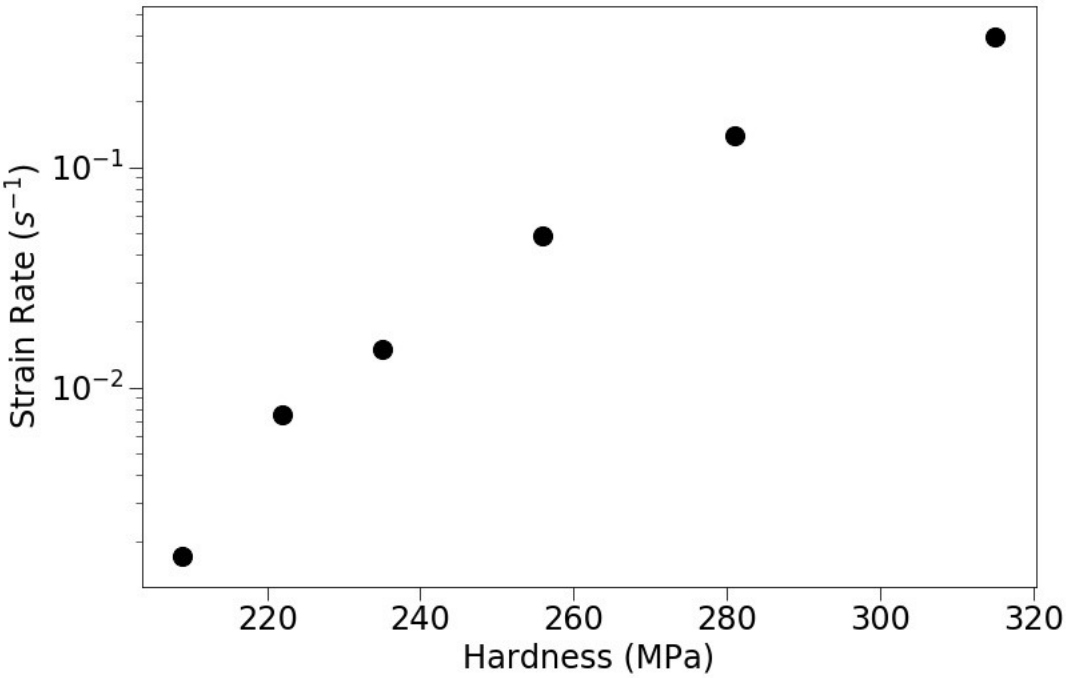

FIGURE 5.3: Plot of steady-state hardness vs. indentation strain rate for 6 target strain rates. Each data point was selected for a depth of 4000 nm, where the indentation-size effect, prominent at shallower depths, is negligible. Error bars representing the variation between all experiments at a given strain rate are smaller than the data points. The stress exponent, i.e., the slope of a line through the data points in the figure, is roughly 25, indicating that plasticity is the dominant deformation mechanism at these conditions.

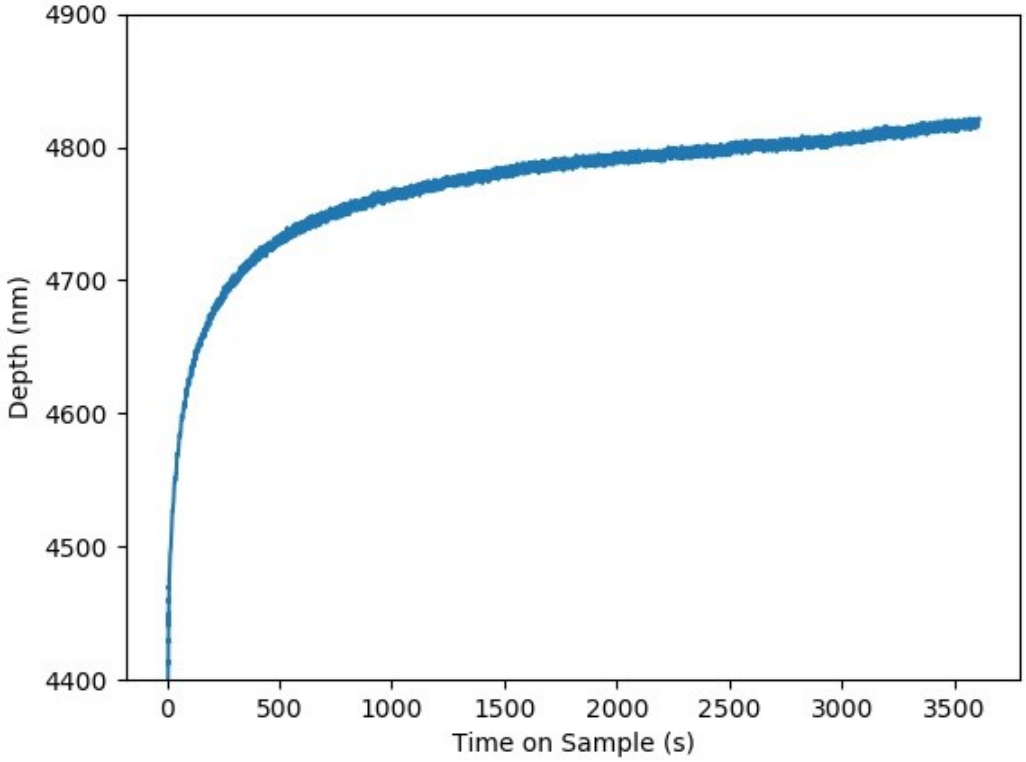

FIGURE 5.4: Plot of the variation of indentation depth with time in a 3600-s creep test. At the beginning of the hold, the displacement rate is larger because the stress on the sample is higher. As the contact area increases due to creep of the sample, the stress on the sample, and thus the displacement rate, decreases. Towards the end of the test, the apparent acceleration in the creep rate (the increase in slope of the curve) is caused by thermal drift of the instrument.

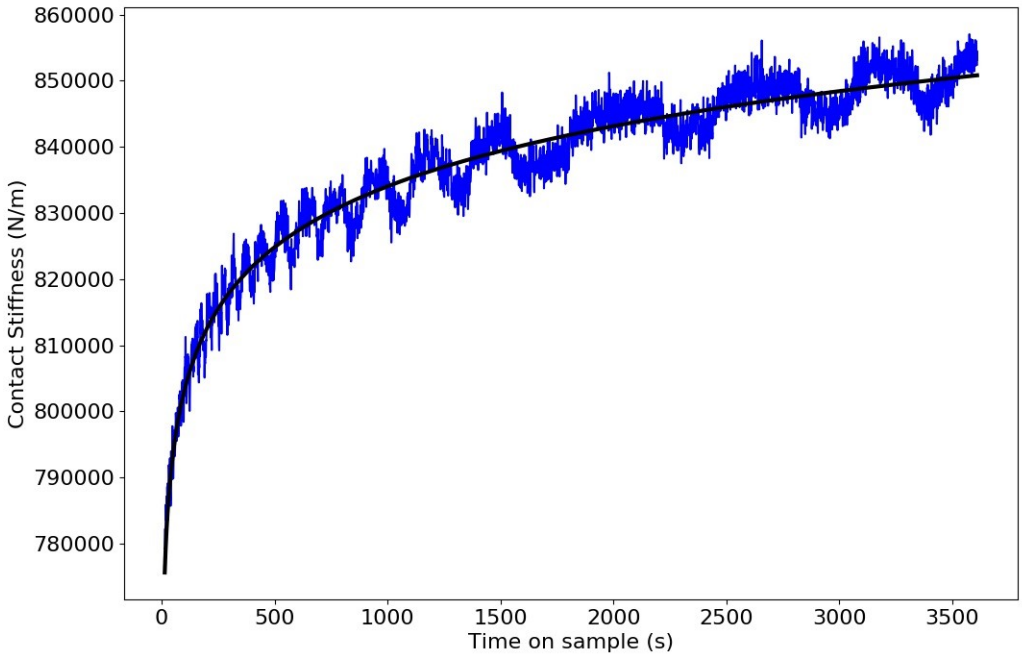

FIGURE 5.5: Plot of contact stiffness vs. time for the same test as shown in Fig. 5.4. The contact stiffness data obtained using the CSM are shown in blue. Although these data appear to be noisy and oscillatory, they are a more accurate measure of the deformation than the displacement data, because of their insensitivity to thermal drift. A smoothed fit to the data is shown in black, but we use the unfiltered data in all subsequent analyses.

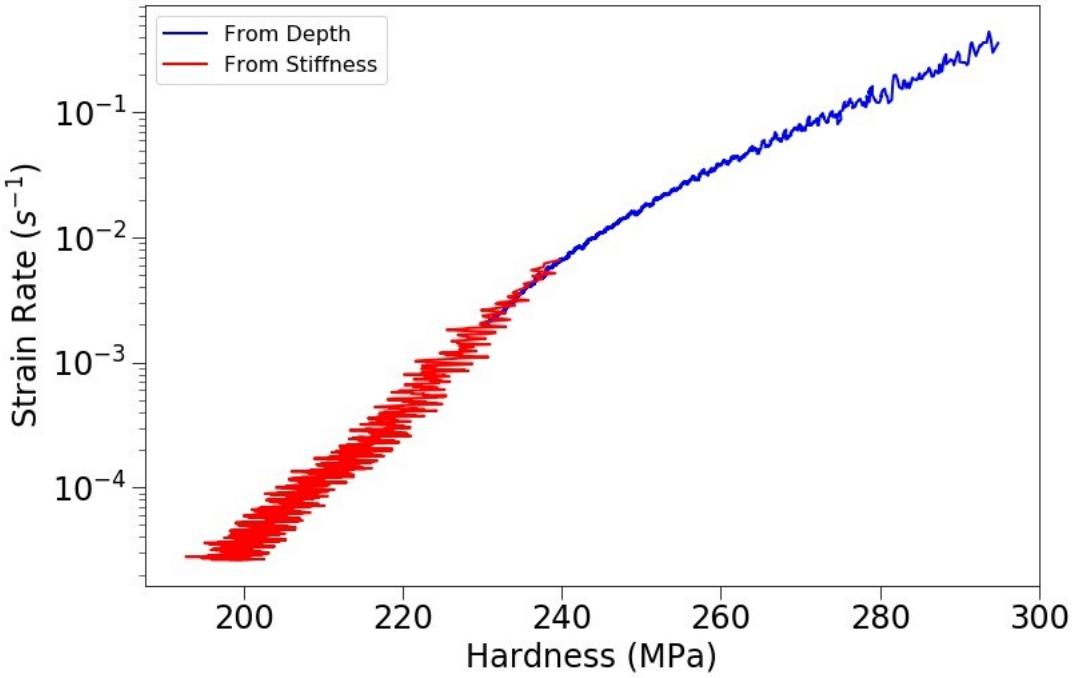

FIGURE 5.6: Plot of indentation strain rate vs. hardness for a 3600-s test (derived from the data shown in Figs. 5.4 and 5.5). The hardness and strain rate for the blue data are determined from the displacement data from the first 10 s of the test, a time scale too short for significant thermal drift. For the remainder of the test, the hardness and strain rate are determined from the contact stiffness, shown in red, which is independent of thermal drift.

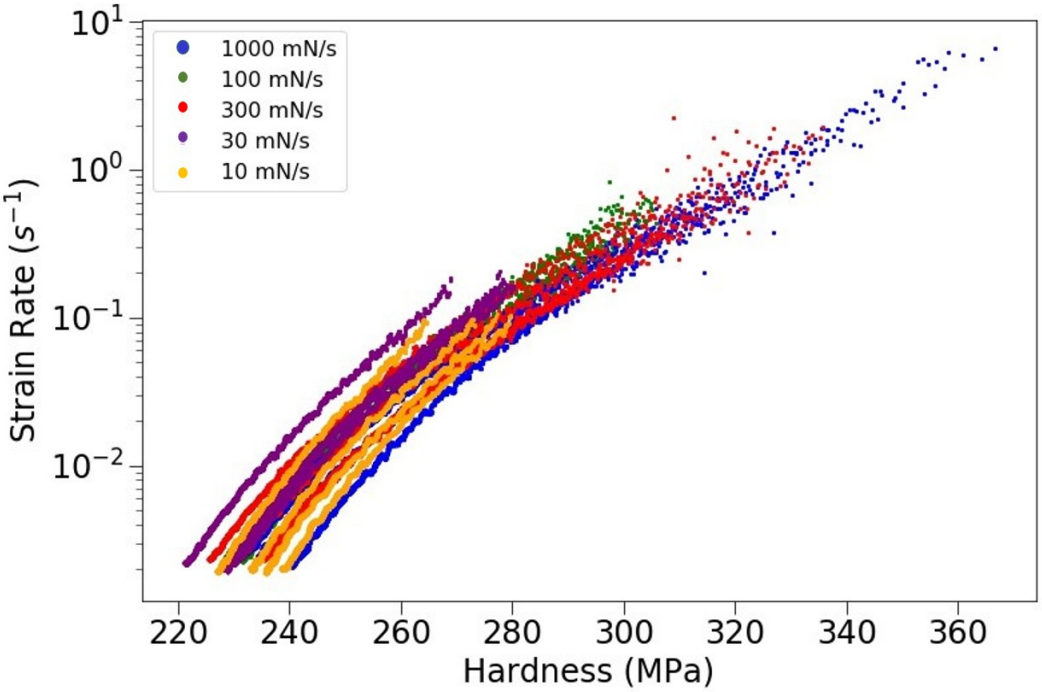

FIGURE 5.7: Plot of hardness vs. strain rate, derived from displacement data, for all experiments with a peak load of 100 mN. Each color corresponds to a different loading rate. No systematic differences are observed in the data, indicating that loading rate does not influence creep behavior during the hold at constant load.

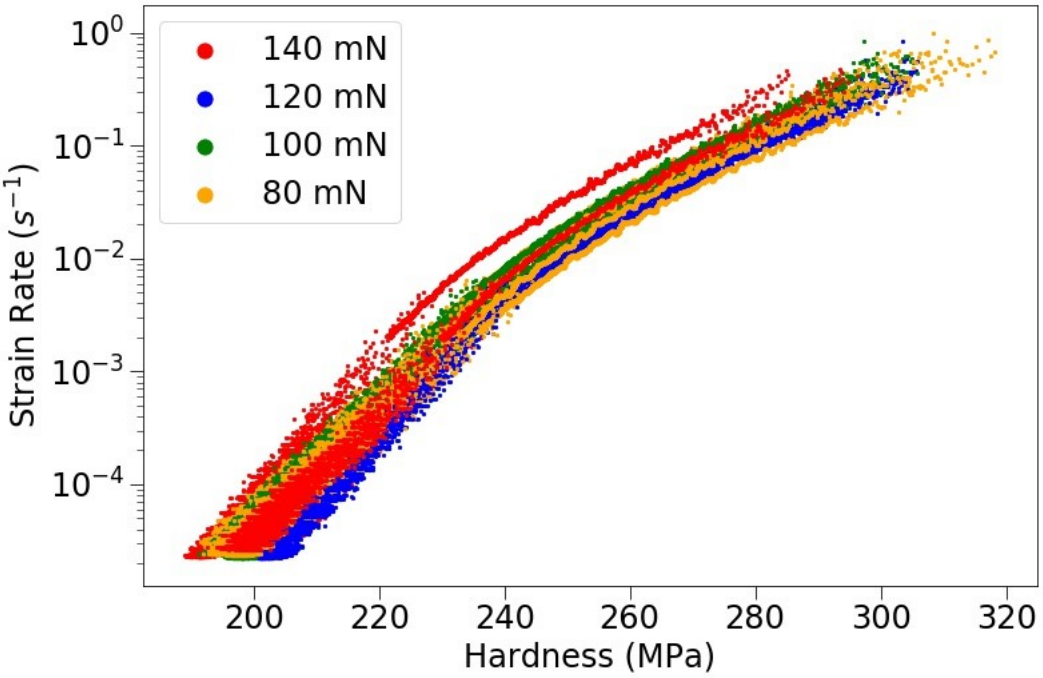

FIGURE 5.8: Plot of hardness vs. strain rate for all experiments performed at a loading rate of 100 mN/s. Data shown here are derived from both displacement measurements (the high-stress portions of the curve) and contact stiffness measurements (the low-stress portions). Each color corresponds to a different maximum load during the hold. All experiments reveal similar behavior over the range of conditions tested.

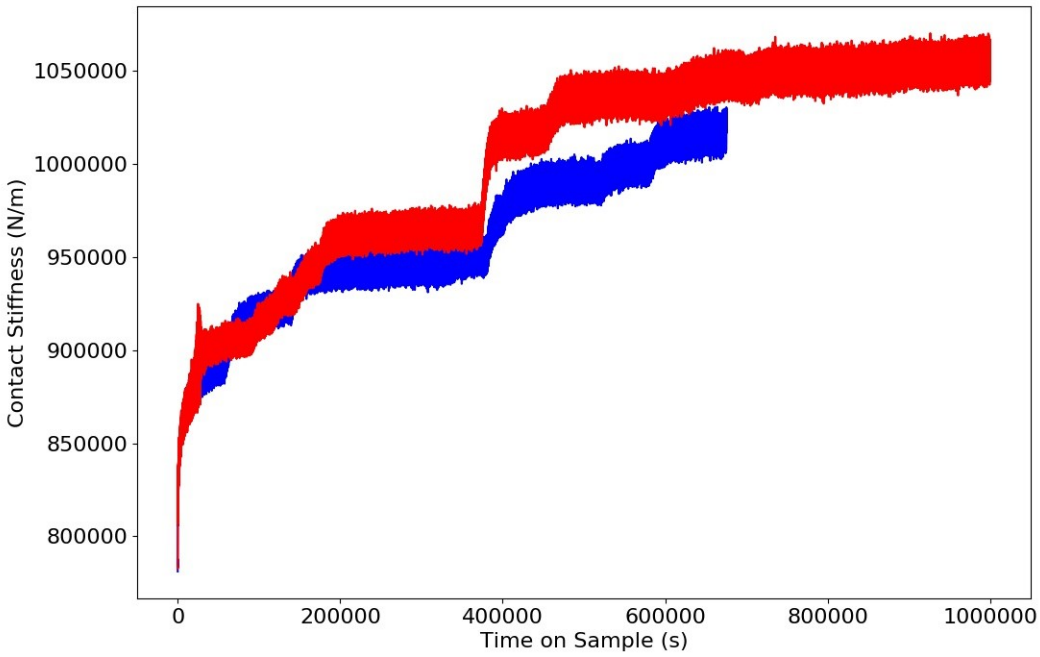

FIGURE 5.9: Plot of contact stiffness obtained via the CSM vs. time for two very-long hold creep tests. Data in the first ∼30,000 s are quantitatively similar to those from other experiments of shorter durations, but marked accelerations and decelerations in the creep rate are observed in both of these experiments at longer hold times.

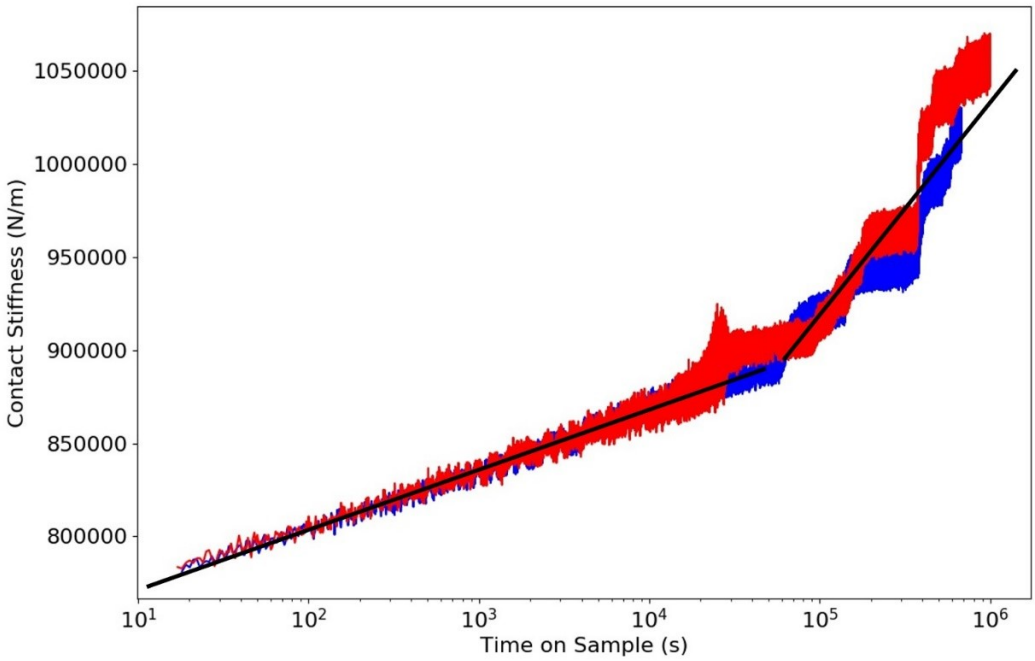

FIGURE 5.10: Plot of the same data as in Fig. 5.9, but with time plotted on a logarithmic scale. A steady increase in the contact stiffness is observed for the first ∼30,000 s of the test, as observed by the linear fit through the data. However, at longer times, there is a sharp change in the the rate of contact stiffness increase, and deformation is unsteady.

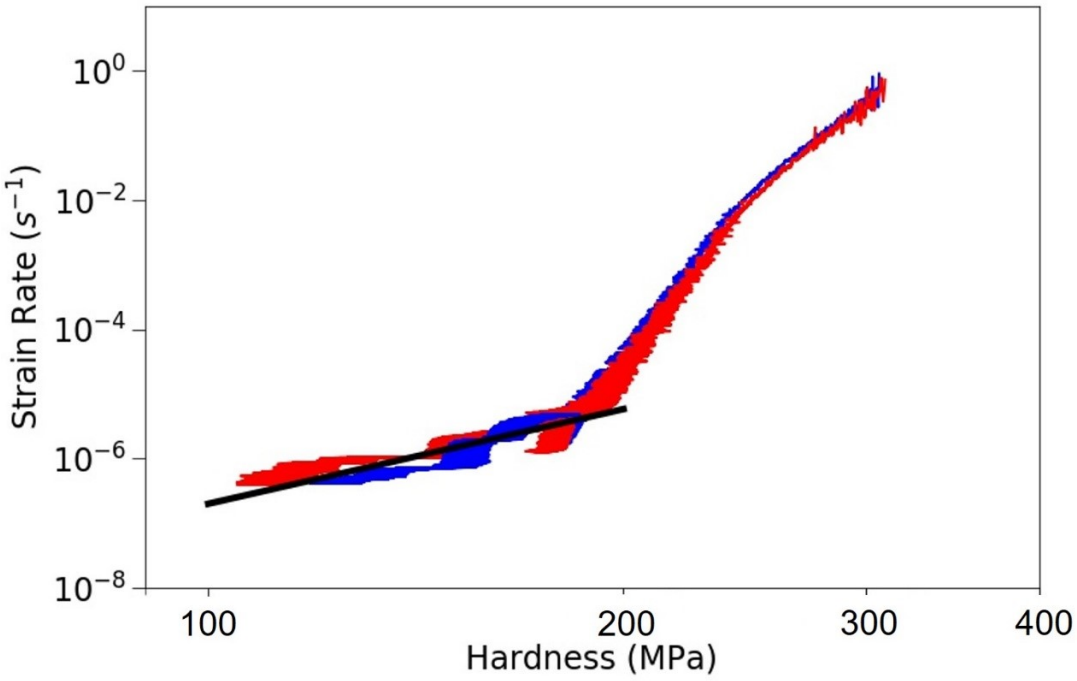

FIGURE 5.11: Hardness vs. strain rate data for the two very-long hold experiments which yielded the data shown in Figs. 5.9 and 5.10. The black line is a best fit to the data at low stress, yielding a slope of 4.87 ± 0.91.

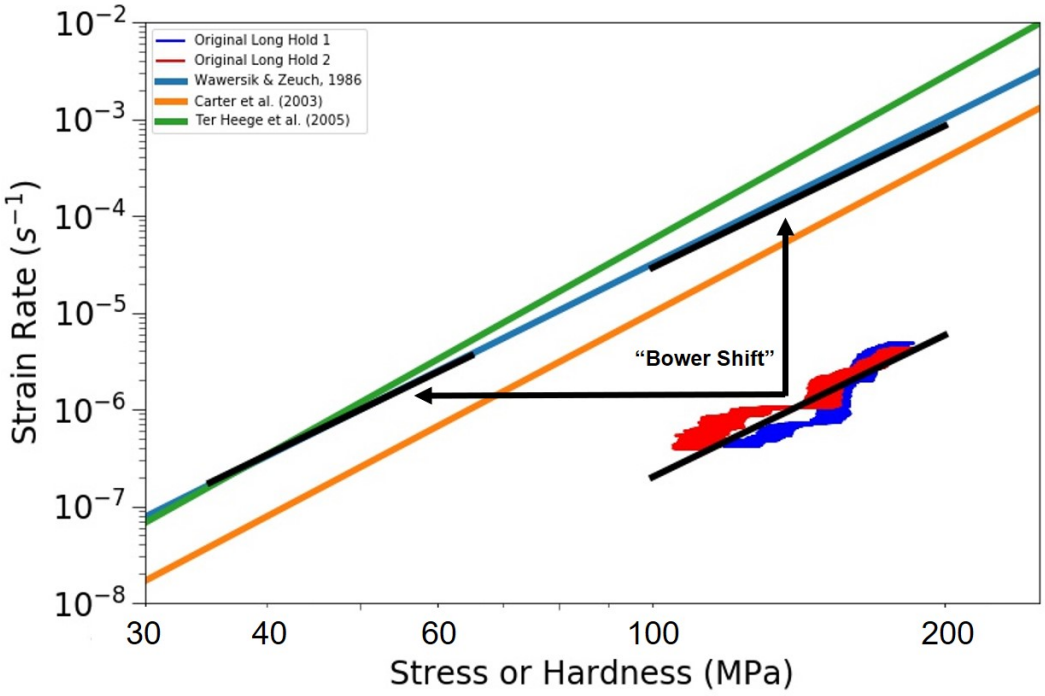

FIGURE 5.12: Plot of stress vs. strain rate illustrating the "Bower shift." The raw data corresponding to the low-stress portions of the long-hold creep tests (where $n = 4.87$) are shown. Three different dislocation creep flow laws extrapolated to room temperature are shown for comparison. The black line, a fit to the raw data, is shifted according to Eq. 5.12, either in the vertical or, equivalently, the horizontal direction. The two shifted black curves agree well with the predictions of the flow laws, particularly that of Wawersik and Zeuch, 1986.

Chapter 6

Conclusions and Future Directions

6.1 Summary and Conclusions

In this thesis, we have measured the room temperature, length-scale dependent plastic deformation of quartz, olivine, halite, and natural fault surfaces using nanoindentation. In addition, the nanoindentation creep behavior of quartz and halite was extensively studied and compared to predictions made from other types of experiments. In short, this dissertation demonstrates that nanoindentation can be used to measure the deformation of geologic materials at room temperature, and, in the future, at high temperature.

6.1.1 Indentation Size Effects

We have identified two different types of indentation size effects, both of which result in a "smaller is stronger" behavior. The first type of size effect is observed in single crystals of olivine (Fig. 3.3) using spherical indenters. Upon loading the sample, the deformation is initially elastic until a sudden stress drop occurs and plastic deformation begins (Fig. 3.2). The stress at which this "pop-in" occurs appears to be stochastic, and it is thought to be caused by a random distribution of dislocation sources. As the size of the stressed volume increases, the likelihood of encountering a distributed dislocation source increases. Therefore, the maximum stress that can be reached decreases as the size of the indenter

increases. If a large enough indenter is used, no nanoindentation pop-ins would be observed because the likelihood of activating a dislocation source is high and deformation would occur at the non-source-limited yield stress.

The second type of indentation size effect is observed in olivine (Fig. 3.3), quartz (Fig. 4.1), halite (Fig. 5.2), and natural faults (Fig. 2.3). This size effect is typically observed for Berkovich (sharp) indenters, but it is also observed in olivine with spherical indenters after a pop-in event. This size effect is due to strain gradients and geometrically necessary dislocations, which create short- and long-range stress fields within the deforming region (e.g. Nix and Gao, 1998; Pharr, Herbert, and Gao, 2010; Kumamoto et al., 2017). As the volume of the deforming material decreases, the density of dislocations must increase for the equivalent amount of strain (a Berkovich tip is self-similar with 8% strain at all indentation depths). This results in a "Taylor hardening" behavior where dislocations strongly interact with each other, thereby increasing the measured hardness of the material.

In this thesis, two important implications of indentation size effects are shown. First, for a natural fault surface, where self-affine roughness is created through frictional sliding and repetitive wear, we show that the scale-dependent strength of natural faults quantitatively agrees with predictions inferred from measurements of scale-dependent roughness (Brodsky, Kirkpatrick, and Candela, 2016; Thom et al., 2017; Chapter 2). Thus, the "steady-state" roughness exhibited on many faults at small length scales is ultimately a result of scale-dependent plastic strength of geologic materials. This geometry can be predicted from the material properties of the fault itself.

The second implication of the size effects shown in this thesis is related to the extrapolation of laboratory-derived plastic flow laws for olivine deforming in Earth's mantle. The maximum strength of oceanic lithosphere is determined by the competition between depth-dependent frictional strength at shallower depths and temperature dependent bulk plastic deformation of olivine deeper in the Earth (e.g. Kohlstedt, Evans, and Mackwell, 1995; Mei et al., 2010). Most experiments to measure olivine plasticity use samples with a

fine grain size for practical purposes, rather than the mm- to cm-sized grain sizes that exist in the upper mantle. The identification of an indentation size effect in olivine suggests that the coarse-grained upper mantle is much weaker than predicted previously. We have conducted a number of experiments to test this prediction (not presented here). Accounting for this size effect brings laboratory predictions into better agreement with geophysical models of plate tectonics and estimates of peak strength based on plate flexure around volcanic islands such as Hawaii (Kumamoto et al., 2017; See Chapter 3 of this dissertation).

6.1.2 Nanoindentation Creep

Room-temperature nanoindentation creep of halite and quartz was extensively studied in this dissertation. In halite, tests were conducted with hold times of up to 10^6 seconds, which identified a change in the dominant deformation mechanism, from plasticity (stress exponent of ≈ 25) to dislocation creep (stress exponent ≈ 5). Using a theoretical analysis developed by Bower et al., 1993, we showed that data derived from a nanoindentation creep test can be directly compared to experiments using more traditional testing geometries. Data from our experiments, when properly treated, agree within 5% of commonly cited flow laws for halite in the dislocation creep regime (e.g., Wawersik and Zeuch, 1986).

Nanoindentation creep tests on quartz were performed as a function of relative humidity in three different nanoindenters, yielding quantitatively similar data that constrain the physical mechanism of frictional aging, as described below.

6.1.3 The Physical Origin of Frictional Aging

A long-standing question in geophysics is whether the time-dependent increase in friction for two surfaces held in quasi-stationary contact, called frictional aging, is due to an increase in the real area of contact due to creep of asperities ("contact quantity") or due to an increase in the amount of chemical bonding across the frictional interface ("contact quality"). Experiments in very low relative humidity conditions have demonstrated that

frictional aging is suppressed (Dieterich and Conrad, 1984; Frye and Marone, 2002), suggesting that the underlying mechanism of aging depends on water. The commonly accepted hypothesis is that creep of asperities is enhanced by water and that aging is due to an increase in contact quantity caused by asperity creep. We have performed creep tests over a wide range of relative humidity to test this hypothesis. Our experiments show no effect of humidity on the yield stress or creep or quartz, demonstrating that changes in contact area alone cannot explain frictional aging. Instead, our results argue for time-dependent chemical bonding across the interface, or some other mechanism such as slip-induced strengthening, as the origin of frictional aging. Our experiments help to constrain the underlying physics of the rate and state friction equation to model earthquake nucleation and recurrence, allowing for more accurate extrapolations from the laboratory to natural conditions.

6.2 Implications and Future Directions

This dissertation has answered questions concerning the room temperature deformation of geologic materials and the utility of nanoindentation in geoscience, as well as constrained important questions concerning the origins of frictional sliding on faults, but a large number of questions and new avenues of research still remain.

Natural fault surfaces have roughness over a wide range of length scales, as shown in Chapter 2. A simple estimate of the mean contact pressure acting on asperities was shown in this dissertation, but a number of future experiments and simulations could improve on this work. For example, predictions about the size distribution and spatial correlation of asperities are made by contact mechanics theories, but these have not been tested for natural fault surfaces. Because these surfaces display remarkably consistent self-affine roughness over many decades of length scale, they are excellent candidates to test these predictions and elucidate more information about the underlying physics of friction.

None of the indentation experiments presented in this dissertation were conducted with an additional shear load, which will change the stress state and affect the deformation of the sample beneath the indenter tip. Shear loading would be more representative of the type of stress felt by asperities on a fault surface, which are inferred to be loaded nearly to failure, and also of asperities loaded in shear in the slide-hold-slide tests used to measure frictional aging. These experiments will be possible in the near future with advances in nanoindentation technology.

Determining whether the shear stress needed to initiate sliding for a single asperity is scale-dependent is a crucial outstanding question raised by this dissertation. We have identified an indentation size effect in the plastic deformation of geologic materials loaded in the normal direction, but this does not necessarily imply that the shear stress needed to slide is also scale-dependent. If the shear stress per unit of area of contact needed to slide is constant, the potential for a scale-dependent friction coefficient exists. If there is indeed a size effect in the shear stress needed to slide, then the friction coefficient for a plastically deforming asperity may be constant, despite the both deformation and shear resistance depending on length scale. Both of these results warrant further study.

Finally, potentially the most important future work following on from this dissertation is the use of high temperature nanoindenters. This technology is currently under development, and many of the experiments performed here can be repeated at elevated temperatures to gain valuable data, such as the activation energies for various creep mechanisms, to understand deformation in geologic materials.

Appendix A

Chapter 2 Supplemental Information

A version of this appendix was previously published as the supplemental information for **Thom, C.A.**, Brodsky, E.E., Carpick, R.W., Pharr, G.M., Oliver, W.C., and Goldsby, D.L. (2017), Nanoscale roughness of natural fault surfaces controlled by scale-dependent yield strength. *Geophysical Research Letters* **44** (18), 9299-9307. doi:10.1002/2017GL074663

A.1 Intermittent Contact Mode Atomic Force Microscopy

To measure the topography of the Corona Heights Fault, we used intermittent contact mode atomic force microscopy (AFM). In intermittent contact mode, the AFM cantilever is oscillated near its resonant frequency ($\sim$300 kHz) as it is dragged across the sample surface. A force feedback loop maintains a constant force on the AFM tip by moving the cantilever vertically (in the z-direction) to mirror the sample topography. Resolution using this method is sub-nm in the z-direction and approaching the radius of curvature ($\sim$10-20 nm) of the AFM tip in the x-y directions. We use a cutoff threshold of 60 nm in this study to avoid the introduction of instrumental artifacts that can occur when attempting to measure topography of order the tip radius [Jacobs, Junge, and Pastewka, 2017].

A.2 Nanoindentation Test Protocol

A typical experiment consisted of three parts. First, the load was increased to the target load of either 200 or 1000 mN for the Yair and Corona Heights Faults, respectively. Second, the indenter tip was held at peak load for 1 s. Finally, the indenter tip was unloaded to 10% of the peak load and held for 90 s to measure the thermal drift rate of the tip displacement. Data were excluded if the thermal drift rate exceeded 0.10 nm/s.

A.3 Continuous Stiffness Method

Traditional nanoindentation techniques determine the contact stiffness from the slope of the initial portion of the unloading curve and use this value of stiffness to calculate hardness and elastic modulus [Oliver and Pharr, 1992]. In order to measure mechanical properties as a function of depth, we utilized the continuous stiffness method. In these experiments, a $\sim$100-Hz sinusoidal oscillation of the indenter force was superimposed on the nominal load such that the resulting displacement oscillation of the tip was maintained at a constant value of 5-nm by means of feedback control. The amplitudes of the oscillatory force and displacement, and the phase lag between them, were then used to determine the contact stiffness over timescales for which thermal drift is negligible [Li and Bhushan, 2002; Oliver and Pharr, 2004]. From the contact stiffness and total depth of penetration, we obtain a measurement of the contact depth, allowing us to calculate the projected area of contact and therefore, the hardness (load divided by projected area of contact).

A.4 Converting Hardness to Yield Stress

To convert indentation hardness to yield stress for a sharp indenter such as the Berkovich, the geometry of the indenter, the elastic modulus of the material, and the hardness must be known. The ratio of hardness, H, to yield stress, σ, is the constraint factor, C. For an indent

accommodated entirely by plastic deformation, $C \approx 3$, and for a fully elastic contact just before yield, $C \approx 1$ [Johnson, 1970]. Because of the sharp tip geometry of the Berkovich, a significant portion of both elastic and plastic deformation occurs. To calculate C in our experiments, we used of the equation from Evans and Goetze, 1979, a correction of the original equation by Johnson, 1970:

$$C = \frac{H}{\sigma} = 0.19 + 1.6 \cdot log\frac{E_S \cdot tan(\phi)}{\sigma} \tag{A.1}$$

Here, E_s is the Young's modulus of the sample determined in the indentation test and ϕ is the angle between the indenter and the sample surface (19.7° for a Berkovich tip).

A.5 Power Spectral Density

Power spectral density can be a confusing term due to inconsistency in its definition, units, and usage across various fields [Jacobs, Junge, and Pastewka, 2017]. In Chapter 2, we have shown the 1-dimensional power spectral density in Figure 2.2 in order to be consistent with several previous fault roughness studies. The power spectral density calculation involves three steps. First, the autocorrelation function is determined along 2-dimensional topographic profiles of our AFM scans. Second, the Fourier power spectrum is determined by calculating the squares of the coefficients of the Fourier transform. Finally, the power spectrum is normalized by the profile length. For an AFM image, this process is repeated for every line of data. Power spectral density curves shown in Figure 2.2 are the subsequent averaging of every line of data in an AFM scan.

A.6 Calculation of Root-Mean-Squared Surface Slope

The root-mean-squared (RMS) slope of a surface can be directly calculated from the 2-dimensional power spectral density, which is the Fourier transform of the autocorrelation

function along both the x- and y-axis [Persson, 2001; Persson, 2006; Persson, 2014]. If the surface is isotropic, the 2-dimensional power spectral density, *C(q)*, can be calculated as

$$C(\mathbf{q}) = \frac{1}{(2\pi)^2} \int d^2x < h(\mathbf{x})h(\mathbf{0}) > e^{-i\mathbf{q}\cdot\mathbf{x}} \tag{A.2}$$

where **q** is the wavevector, *h(**x**)* is the height coordinate of a point in the x-y plane, and <..> represents ensemble averaging [Persson, 2014]. If the surface is self-affine from a small wavevector cutoff, q_0, to a large wavevector cutoff, q_1, then the mean pressure can be directly related to the RMS slope at the smallest length scale (i.e. corresponding to wavevector q_1). In this case, the power spectral density can be expressed as

$$C(q) = C_0 \left(\frac{q_1}{q_0}\right)^{-2(1+\zeta)} \tag{A.3}$$

where ζ is the Hurst exponent. The RMS slope, <*dh/dx*>, is determined by

$$< \frac{dh}{dx} >= \left(2\pi \int_{q_0}^{q_1} dq q^3 C(q)\right)^{0.5} \tag{A.4}$$

From Equation A.3 and Equation A.4, Persson, 2014 shows

$$< \frac{dh}{dx} >= \left(\frac{\pi C_0}{1-\zeta} q_0^4 \left[\left(\frac{q_1}{q_0}\right)^{2(1-\zeta)} - 1\right]\right)^{0.5} \tag{A.5}$$

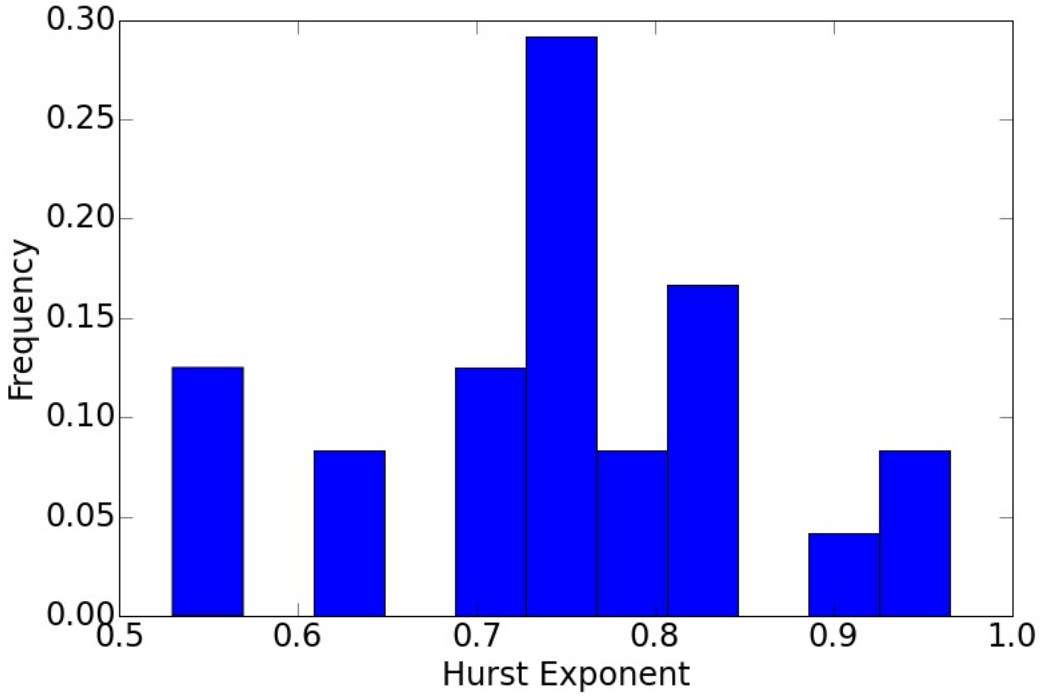

FIGURE A.1: Histogram of the Hurst exponents for each individual AFM scan on the Corona Heights Fault.

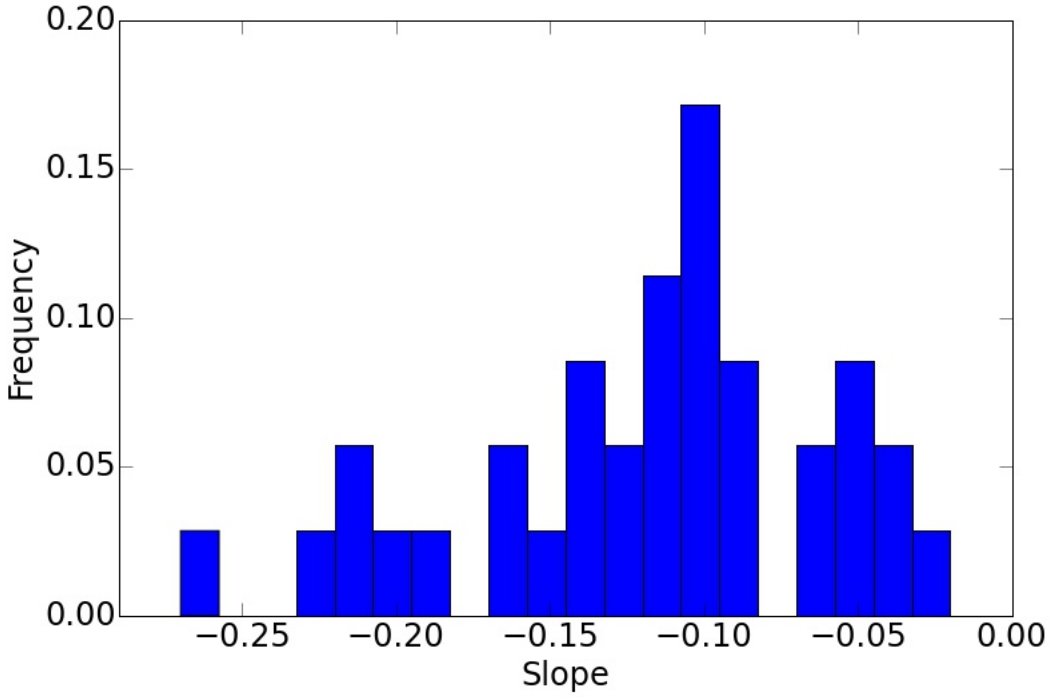

FIGURE A.2: Histogram of the best-fit values of the power-law exponent for all tests on the Corona Heights Fault.

Bibliography

Abramson, EH et al. (1997). "The elastic constants of San Carlos olivine to 17 GPa". In: *Journal of Geophysical Research: Solid Earth* 102.B6, pp. 12253–12263.

Ampuero, Jean-Paul and Allan M Rubin (2008). "Earthquake nucleation on rate and state faults–Aging and slip laws". In: *Journal of Geophysical Research: Solid Earth* 113.B1.

Andreev, George E (1995). *Brittle failure of rock materials*. CRC Press.

Bai, Quart, SJ Mackwell, and DL Kohlstedt (1991). "High-temperature creep of olivine single crystals 1. Mechanical results for buffered samples". In: *Journal of Geophysical Research: Solid Earth* 96.B2, pp. 2441–2463.

Bandis, S, AC Lumsden, and NR Barton (1981). "Experimental studies of scale effects on the shear behaviour of rock joints". In: *International journal of rock mechanics and mining sciences & geomechanics abstracts*. Vol. 18. 1. Elsevier, pp. 1–21.

Behn, Mark D, Greg Hirth, and James R Elsenbeck II (2009). "Implications of grain size evolution on the seismic structure of the oceanic upper mantle". In: *Earth and Planetary Science Letters* 282.1-4, pp. 178–189.

Berest, P and B Brouard (1998). "A tentative classification of salts according to their creep properties". In: *Proceeding of SMRI spring meeting, New Orleans, Louisiana, USA, April*, pp. 19–22.

Bhattacharya, Pathikrit, Allan M Rubin, and Nicholas M Beeler (2017). "Does fault strengthening in laboratory rock friction experiments really depend primarily upon time and not slip?" In: *Journal of Geophysical Research: Solid Earth* 122.8, pp. 6389–6430.

Boettcher, Margaret S, Greg Hirth, and Brian Evans (2007). "Olivine friction at the base of oceanic seismogenic zones". In: *Journal of Geophysical Research: Solid Earth* 112.B1.

Bonamy, Daniel and Elisabeth Bouchaud (2011). "Failure of heterogeneous materials: a dynamic phase transition?" In: *Physics Reports* 498.1, pp. 1–44.

Bouchaud, E and S Navéos (1995). "From quasi-static to rapid fracture". In: *Journal de Physique I* 5.5, pp. 547–554.

Bouchaud, Elisabeth (1997). "Scaling properties of cracks". In: *Journal of Physics: Condensed Matter* 9.21, p. 4319.

Bouchbinder, Eran, Joachim Mathiesen, and Itamar Procaccia (2004). "Roughening of fracture surfaces: the role of plastic deformation". In: *Physical review letters* 92.24, p. 245505.

Bowden, FP and D Tabor (1954). "The Friction and Lubrication of Solids (Clarendon, Oxford)". In:

Bower, AF et al. (1993). "Indentation of a power law creeping solid". In: *Proc. R. Soc. Lond. A* 441.1911, pp. 97–124.

Brace, WF (1963). "Behavior of quartz during indentation". In: *The Journal of Geology* 71.5, pp. 581–595.

Brodsky, Emily E, James D Kirkpatrick, and Thibault Candela (2016). "Constraints from fault roughness on the scale-dependent strength of rocks". In: *Geology* 44.1, pp. 19–22.

Brodsky, Emily E et al. (2011). "Faults smooth gradually as a function of slip". In: *Earth and Planetary Science Letters* 302.1-2, pp. 185–193.

Brown, Stephen R and Christopher H Scholz (1985). "Broad bandwidth study of the topography of natural rock surfaces". In: *Journal of Geophysical Research: Solid Earth* 90.B14, pp. 12575–12582.

Buffett, BA and TW Becker (2012). "Bending stress and dissipation in subducted lithosphere". In: *Journal of Geophysical Research: Solid Earth* 117.B5.

Bull, SJ, Trevor F Page, and EH Yoffe (1989). "An explanation of the indentation size effect in ceramics". In: *Philosophical Magazine Letters* 59.6, pp. 281–288.

Bush, AW, RD Gibson, and TR Thomas (1975). "The elastic contact of a rough surface". In: *Wear* 35.1, pp. 87–111.

Candela, Thibault and Emily E Brodsky (2016). "The minimum scale of grooving on faults". In: *Geology* 44.8, pp. 603–606.

Candela, Thibault et al. (2009). "Characterization of fault roughness at various scales: Implications of three-dimensional high resolution topography measurements". In: *Mechanics, Structure and Evolution of Fault Zones*. Springer, pp. 1817–1851.

Candela, Thibault et al. (2011). "Fault slip distribution and fault roughness". In: *Geophysical Journal International* 187.2, pp. 959–968.

Candela, Thibault et al. (2012). "Roughness of fault surfaces over nine decades of length scales". In: *Journal of Geophysical Research: Solid Earth* 117.B8.

Carter, Neville L and Francis D Hansen (1983). "Creep of rocksalt". In: *Tectonophysics* 92.4, pp. 275–333.

Carter, NL et al. (1993). "Rheology of rocksalt". In: *Journal of Structural Geology* 15.9-10, pp. 1257–1271.

Chen, Xiaofeng et al. (2013). "Dynamic weakening by nanoscale smoothing during high-velocity fault slip". In: *Geology* 41.7, pp. 739–742.

Chester, Frederick M (1988). "The brittle-ductile transition in a deformation-mechanism map for halite". In: *Tectonophysics* 154.1-2, pp. 125–136.

Chromik, RR et al. (2003). "Nanoindentation measurements on Cu–Sn and Ag–Sn intermetallics formed in Pb-free solder joints". In: *Journal of Materials Research* 18.9, pp. 2251–2261.

Demouchy, Sylvie et al. (2013). "Low strength of Earth's uppermost mantle inferred from tri-axial deformation experiments on dry olivine crystals". In: *Physics of the Earth and Planetary Interiors* 220, pp. 37–49.

Demouchy, Sylvie et al. (2014). "Viscoplasticity of polycrystalline olivine experimentally deformed at high pressure and 900 C". In: *Tectonophysics* 623, pp. 123–135.

Dieter, George Ellwood and David J Bacon (1986). *Mechanical metallurgy*. Vol. 3. McGraw-hill New York.

Dieterich, James H (1972). "Time-dependent friction in rocks". In: *Journal of Geophysical Research* 77.20, pp. 3690–3697.

— (1979). "Modeling of rock friction: 1. Experimental results and constitutive equations". In: *Journal of Geophysical Research: Solid Earth* 84.B5, pp. 2161–2168.

— (1992). "Earthquake nucleation on faults with rate-and state-dependent strength". In: *Tectonophysics* 211.1-4, pp. 115–134.

Dieterich, James H and Gerald Conrad (1984). "Effect of humidity on time-and velocity-dependent friction in rocks". In: *Journal of Geophysical Research: Solid Earth* 89.B6, pp. 4196–4202.

Dieterich, James H and Brian D Kilgore (1994). "Direct observation of frictional contacts: New insights for state-dependent properties". In: *Pure and Applied Geophysics* 143.1-3, pp. 283–302.

Druiventak, Anthony et al. (2011). "Low-temperature plasticity of olivine during high stress deformation of peridotite at lithospheric conditions—An experimental study". In: *Earth and Planetary Science Letters* 311.3-4, pp. 199–211.

Dunstan, DJ and AJ Bushby (2014). "Grain size dependence of the strength of metals: the Hall–Petch effect does not scale as the inverse square root of grain size". In: *International Journal of Plasticity* 53, pp. 56–65.

Durham, WB, C Goetze, and B Blake (1977). "Plastic flow of oriented single crystals of olivine: 2. Observations and interpretations of the dislocation structures". In: *Journal of Geophysical Research* 82.36, pp. 5755–5770.

Durst, Karsten, Björn Backes, and Mathias Göken (2005). "Indentation size effect in metallic materials: correcting for the size of the plastic zone". In: *Scripta Materialia* 52.11, pp. 1093–1097.

Evans, Brian (1984). "The effect of temperature and impurity content on indentation hardness of quartz". In: *Journal of Geophysical Research: Solid Earth* 89.B6, pp. 4213–4222.

Evans, Brian and Christopher Goetze (1979). "The temperature variation of hardness of olivine and its implication for polycrystalline yield stress". In: *Journal of Geophysical Research: Solid Earth* 84.B10, pp. 5505–5524.

Faul, Ulrich H et al. (2011). "Dislocation creep of fine-grained olivine". In: *Journal of Geophysical Research: Solid Earth* 116.B1.

Fossum, ARLO F and JOANNE T Fredrich (2002). *Salt mechanics primer for near-salt and sub-salt deepwater Gulf of Mexico field developments*. Sandia National Laboratories Albuquerque, New Mexico, and Livermore, California.

Franssen, Raymond CMW (1994). "The rheology of synthetic rocksalt in uniaxial compression". In: *Tectonophysics* 233.1-2, pp. 1–40.

Frye, Kevin M and Chris Marone (2002). "Effect of humidity on granular friction at room temperature". In: *Journal of Geophysical Research: Solid Earth* 107.B11.

Ginder, Ryan S, William D Nix, and George M Pharr (2018). "A simple model for indentation creep". In: *Journal of the Mechanics and Physics of Solids* 112, pp. 552–562.

Goldsby, David L et al. (2004). "Nanoindentation creep of quartz, with implications for rate-and state-variable friction laws relevant to earthquake mechanics". In: *Journal of materials research* 19.1, pp. 357–365.

Greenwood, JA and JB Pl Williamson (1966). "Contact of nominally flat surfaces". In: *Proc. R. Soc. Lond. A* 295.1442, pp. 300–319.

Greer, Julia R, Warren C Oliver, and William D Nix (2005). "Size dependence of mechanical properties of gold at the micron scale in the absence of strain gradients". In: *Acta Materialia* 53.6, pp. 1821–1830.

Gu, Ji-Cheng et al. (1984). "Slip motion and stability of a single degree of freedom elastic system with rate and state dependent friction". In: *Journal of the Mechanics and Physics of Solids* 32.3, pp. 167–196.

Hall, EO (1951). "The deformation and ageing of mild steel: III discussion of results". In: *Proceedings of the Physical Society. Section B* 64.9, p. 747.

Hanneman, RE and JH Westbrook (1968). "Effects of adsorption on the indentation deformation of non-metallic solids". In: *Philosophical magazine* 18.151, pp. 73–88.

Hansen, Alex and Jean Schmittbuhl (2003). "Origin of the universal roughness exponent of brittle fracture surfaces: stress-weighted percolation in the damage zone". In: *Physical review letters* 90.4, p. 045504.

Hansen, LN, ME Zimmerman, and David L Kohlstedt (2011). "Grain boundary sliding in San Carlos olivine: Flow law parameters and crystallographic-preferred orientation". In: *Journal of Geophysical Research: Solid Earth* 116.B8.

Heard, Hugh C (1972). "Steady-state flow in polycrystalline halite at pressure of 2 kilobars". In: *Flow and fracture of rocks* 16, pp. 191–209.

Heard, Hugh Corey and FJ Ryerson (1986). "Effect of cation impurities on steady-state flow of salt". In: *Mineral and Rock Deformation: Laboratory Studies* 36, pp. 99–115.

Hunsche, Udo and Andreas Hampel (1999). "Rock salt—the mechanical properties of the host rock material for a radioactive waste repository". In: *Engineering geology* 52.3-4, pp. 271–291.

Hyun, S et al. (2004). "Finite-element analysis of contact between elastic self-affine surfaces". In: *Physical Review E* 70.2, p. 026117.

Idrissi, Hosni et al. (2016). "Low-temperature plasticity of olivine revisited with in situ TEM nanomechanical testing". In: *Science advances* 2.3, e1501671.

Jackson, Martin PA and Christopher J Talbot (1986). "External shapes, strain rates, and dynamics of salt structures". In: *Geological Society of America Bulletin* 97.3, pp. 305–323.

Jacobs, Tevis DB, Till Junge, and Lars Pastewka (2017). "Quantitative characterization of surface topography using spectral analysis". In: *Surface Topography: Metrology and Properties* 5.1, p. 013001.

Johnson, KL (1970). "The correlation of indentation experiments". In: *Journal of the Mechanics and Physics of Solids* 18.2, pp. 115–126.

— (1985). "Contact Mechanics, 452 pp". In: *Cambridge University, New York*.

Kashani, MS and V Madhavan (2011). "Analysis and correction of the effect of sample tilt on results of nanoindentation". In: *Acta Materialia* 59.3, pp. 883–895.

Kawazoe, Takaaki et al. (2009). "Shear deformation of dry polycrystalline olivine under deep upper mantle conditions using a rotational Drickamer apparatus (RDA)". In: *Physics of the Earth and Planetary Interiors* 174.1-4, pp. 128–137.

Kirkpatrick, JD et al. (2013). "Silica gel formation during fault slip: Evidence from the rock record". In: *Geology* 41.9, pp. 1015–1018.

Kohlstedt, DL, Brian Evans, and SJ Mackwell (1995). "Strength of the lithosphere: Constraints imposed by laboratory experiments". In: *Journal of Geophysical Research: Solid Earth* 100.B9, pp. 17587–17602.

Kranjc, Kelly et al. (2016). "Low-temperature plastic rheology of olivine determined by nanoindentation". In: *Geophysical Research Letters* 43.1, pp. 176–184.

Kumamoto, Kathryn M et al. (2017). "Size effects resolve discrepancies in 40 years of work on low-temperature plasticity in olivine". In: *Science advances* 3.9, e1701338.

Lapusta, Nadia and Yi Liu (2009). "Three-dimensional boundary integral modeling of spontaneous earthquake sequences and aseismic slip". In: *Journal of Geophysical Research: Solid Earth* 114.B9.

Lapusta, Nadia et al. (2000). "Elastodynamic analysis for slow tectonic loading with spontaneous rupture episodes on faults with rate-and state-dependent friction". In: *Journal of Geophysical Research: Solid Earth* 105.B10, pp. 23765–23789.

Lee, Joong-Jeek and Ronald L Bruhn (1996). "Structural anisotropy of normal fault surfaces". In: *Journal of Structural Geology* 18.8, pp. 1043–1059.

Li, Ao, Yun Liu, and Izabela Szlufarska (2014). "Effects of interfacial bonding on friction and wear at silica/silica interfaces". In: *Tribology Letters* 56.3, pp. 481–490.

Li, Qunyang et al. (2011). "Frictional ageing from interfacial bonding and the origins of rate and state friction". In: *Nature* 480.7376, p. 233.

Li, Shiyuan et al. (2012). "Numerical modelling of the displacement and deformation of embedded rock bodies during salt tectonics: A case study from the South Oman Salt Basin". In: *Geological Society, London, Special Publications* 363.1, pp. 503–520.

Li, Xiaodong and Bharat Bhushan (2002). "A review of nanoindentation continuous stiffness measurement technique and its applications". In: *Materials characterization* 48.1, pp. 11–36.

Li, Yuan, Andy J Bushby, and David J Dunstan (2016). "The Hall–Petch effect as a manifestation of the general size effect". In: *Proc. R. Soc. A* 472.2190, p. 20150890.

Linckens, J, G Zulauf, and J Hammer (2016). "Experimental deformation of coarse-grained rock salt to high strain". In: *Journal of Geophysical Research: Solid Earth* 121.8, pp. 6150–6171.

Liu, Yun and Izabela Szlufarska (2012). "Chemical origins of frictional aging". In: *Physical review letters* 109.18, p. 186102.

Long, Hongbo et al. (2011). "Deformation of olivine at subduction zone conditions determined from in situ measurements with synchrotron radiation". In: *Physics of the Earth and Planetary Interiors* 186.1-2, pp. 23–35.

Lucas, BN and WC Oliver (1999). "Indentation power-law creep of high-purity indium". In: *Metallurgical and Materials Transactions A* 30.3, pp. 601–610.

Marone, Chris (1998). "Laboratory-derived friction laws and their application to seismic faulting". In: *Annual Review of Earth and Planetary Sciences* 26.1, pp. 643–696.

Meade, Charles and Raymond Jeanloz (1990). "The strength of mantle silicates at high pressures and room temperature: implications for the viscosity of the mantle". In: *Nature* 348.6301, p. 533.

Mei, S et al. (2010). "Experimental constraints on the strength of the lithospheric mantle". In: *Journal of Geophysical Research: Solid Earth* 115.B8.

Nagata, Kohei et al. (2014). "High-frequency imaging of elastic contrast and contact area with implications for naturally observed changes in fault properties". In: *Journal of Geophysical Research: Solid Earth* 119.7, pp. 5855–5875.

Nix, William D and Huajian Gao (1998). "Indentation size effects in crystalline materials: a law for strain gradient plasticity". In: *Journal of the Mechanics and Physics of Solids* 46.3, pp. 411–425.

Nye, JF (1953). "Some geometrical relations in dislocated crystals". In: *Acta metallurgica* 1.2, pp. 153–162.

Oliver, Warren C and Georges M Pharr (2004). "Measurement of hardness and elastic modulus by instrumented indentation: Advances in understanding and refinements to methodology". In: *Journal of materials research* 19.1, pp. 3–20.

Oliver, Warren Carl and George Mathews Pharr (1992). "An improved technique for determining hardness and elastic modulus using load and displacement sensing indentation experiments". In: *Journal of materials research* 7.6, pp. 1564–1583.

Paterson, Mervyn S and Teng-fong Wong (2005). *Experimental rock deformation-the brittle field*. Springer Science & Business Media.

Pathak, Siddhartha and Surya R Kalidindi (2015). "Spherical nanoindentation stress–strain curves". In: *Materials Science and Engineering: R: Reports* 91, pp. 1–36.

Pearson, DG, D Canil, and SB Shirey (2014). "Mantle samples included in volcanic rocks: xenoliths and diamonds". In:

Pei, L et al. (2005). "Finite element modeling of elasto-plastic contact between rough surfaces". In: *Journal of the Mechanics and Physics of Solids* 53.11, pp. 2385–2409.

Persson, BNJ (2014). "On the fractal dimension of rough surfaces". In: *Tribology Letters* 54.1, pp. 99–106.

Persson, Bo NJ (2001). "Theory of rubber friction and contact mechanics". In: *The Journal of Chemical Physics* 115.8, pp. 3840–3861.

Persson, Bo NJ (2006). "Contact mechanics for randomly rough surfaces". In: *Surface science reports* 61.4, pp. 201–227.

Petch, NJ (1953). "The cleavage strength of polycrystals". In: *Journal of the Iron and Steel Institute* 174, pp. 25–28.

Pharr, George M, Erik G Herbert, and Yanfei Gao (2010). "The indentation size effect: a critical examination of experimental observations and mechanistic interpretations". In: *Annual Review of Materials Research* 40, pp. 271–292.

Pluymakers, Anne, Maya Kobchenko, and François Renard (2017). "How microfracture roughness can be used to distinguish between exhumed cracks and in-situ flow paths in shales". In: *Journal of Structural Geology* 94, pp. 87–97.

Ponson, Laurent, Daniel Bonamy, and Elisabeth Bouchaud (2006). "Two-dimensional scaling properties of experimental fracture surfaces". In: *Physical review letters* 96.3, p. 035506.

Ponson, Laurent et al. (2006). "Anisotropic self-affine properties of experimental fracture surfaces". In: *International Journal of fracture* 140.1-4, pp. 27–37.

Power, William L and Terry E Tullis (1991). "Euclidean and fractal models for the description of rock surface roughness". In: *Journal of Geophysical Research: Solid Earth* 96.B1, pp. 415–424.

Power, William L, Terry E Tullis, and John D Weeks (1988). "Roughness and wear during brittle faulting". In: *Journal of Geophysical Research: Solid Earth* 93.B12, pp. 15268–15278.

Power, WL and WB Durham (1997). "Topography of natural and artificial fractures in granitic rocks: Implications for studies of rock friction and fluid migration". In: *International Journal of Rock Mechanics and Mining Sciences* 34.6, pp. 979–989.

Power, WL et al. (1987). "Roughness of natural fault surfaces". In: *Geophysical Research Letters* 14.1, pp. 29–32.

Proietti, Arnaud et al. (2016). "Effect of pressure on the strength of olivine at room temperature". In: *Physics of the Earth and Planetary Interiors* 259, pp. 34–44.

Raterron, Paul et al. (2004). "Low-temperature olivine rheology at high pressure". In: *Physics of the Earth and Planetary Interiors* 145.1-4, pp. 149–159.

Renard, François, Thibault Candela, and Elisabeth Bouchaud (2013). "Constant dimensionality of fault roughness from the scale of micro-fractures to the scale of continents". In: *Geophysical Research Letters* 40.1, pp. 83–87.

Renard, François, Karen Mair, and Olav Gundersen (2012). "Surface roughness evolution on experimentally simulated faults". In: *Journal of Structural Geology* 45, pp. 101–112.

Renard, François et al. (2006). "High resolution 3D laser scanner measurements of a strike-slip fault quantify its morphological anisotropy at all scales". In: *Geophysical Research Letters* 33.4.

Rice, James R and Glenn E Beltz (1994). "The activation energy for dislocation nucleation at a crack". In: *Journal of the Mechanics and Physics of Solids* 42.2, pp. 333–360.

Sagy, Amir, Emily E Brodsky, and Gary J Axen (2007). "Evolution of fault-surface roughness with slip". In: *Geology* 35.3, pp. 283–286.

Schmittbuhl, Jean, Sylvie Gentier, and Stéphane Roux (1993). "Field measurements of the roughness of fault surfaces". In: *Geophysical Research Letters* 20.8, pp. 639–641.

Schmittbuhl, Jean, Francois Schmitt, and Christopher Scholz (1995). "Scaling invariance of crack surfaces". In: *Journal of Geophysical Research: Solid Earth* 100.B4, pp. 5953–5973.

Schmittbuhl, Jean, Jean-Pierre Vilotte, and Stéphane Roux (1995). "Reliability of self-affine measurements". In: *Physical Review E* 51.1, p. 131.

Schoenherr, J et al. (2007). "Deformation mechanisms and rheology of Pre-cambrian rock-salt from the South Oman Salt Basin". In: *The mechanical behaviour of salt—understanding of THMC processes in salt. Taylor & Francis, London*, pp. 167–173.

Scholz, Christopher H (2002). *The mechanics of earthquakes and faulting*. Cambridge university press.

Senseny, PE et al. (1992). "Mechanical behaviour of rock salt: phenomenology and micromechanisms". In: *International journal of rock mechanics and mining sciences & geomechanics abstracts*. Vol. 29. 4. Elsevier, pp. 363–378.

Shim, S et al. (2008). "A different type of indentation size effect". In: *Scripta Materialia* 59 (10), pp. 1095–1098.

Shimamoto, Toshihiko (1986). "Transition between frictional slip and ductile flow for halite shear zones at room temperature". In: *Science* 231.4739, pp. 711–714.

Shimamoto, Toshihiko and John M Logan (1986). "Velocitydependent behavior of simulated halite shear zones: an analog for silicates". In: *See Das et al* 37, pp. 49–63.

Siman-Tov, Shalev et al. (2013). "Nanograins form carbonate fault mirrors". In: *Geology* 41.6, pp. 703–706.

Skemer, Philip et al. (2009). "Microstructural and rheological evolution of a mantle shear zone". In: *Journal of Petrology* 51.1-2, pp. 43–53.

Skrotzki, W and P Haasen (1988). "The influence of texture on the creep of salt". In: *Proceedings 2nd Conference, Mechanical Behaviour of Salt*, pp. 83–8.

Skrotzki, W and ZG Liu (1982). "Analysis of the cross slip process in alkali halides". In: *physica status solidi (a)* 73.2, K225–K229.

Sneddon, Ian N (1965). "The relation between load and penetration in the axisymmetric Boussinesq problem for a punch of arbitrary profile". In: *International journal of engineering science* 3.1, pp. 47–57.

Spiers, CJ, JL Urai, and GS Lister (1988). "The effect of brine (inherent or added) on rheology and deformation mechanisms in salt rock". In: *Proc. Second Conf. on Mechanical Behavior of Salt. Trans. Tech. Publ., Hanover, W. Germany*, pp. 89–102.

Spiers, CJ et al. (1986). *The influence of fluid-rock interaction on the rheology of salt rock*. Tech. rep. Commission of the European Communities.

Spiers, CJ et al. (1990). "Experimental determination of constitutive parameters governing creep of rocksalt by pressure solution". In: *Geological Society, London, Special Publications* 54.1, pp. 215–227.

Su, Caijun et al. (2013). "Measurement of power-law creep parameters by instrumented indentation methods". In: *Journal of the Mechanics and Physics of Solids* 61.2, pp. 517–536.

Swadener, JG, EP George, and GM Pharr (2002). "The correlation of the indentation size effect measured with indenters of various shapes". In: *Journal of the Mechanics and Physics of Solids* 50.4, pp. 681–694.

Tabor, David (1970). "The hardness of solids". In: *Review of physics in technology* 1.3, p. 145.

Tackley, Paul J (2000a). "Mantle convection and plate tectonics: Toward an integrated physical and chemical theory". In: *Science* 288.5473, pp. 2002–2007.

— (2000b). "Self-consistent generation of tectonic plates in time-dependent, three-dimensional mantle convection simulations". In: *Geochemistry, Geophysics, Geosystems* 1.8.

— (2000c). "The quest for self-consistent generation of plate tectonics in mantle convection models". In: *Geophysical Monograph-American Geophysical Union* 121, pp. 47–72.

Ter Heege, JH, JHP De Bresser, and CJ Spiers (2005). "Rheological behaviour of synthetic rocksalt: the interplay between water, dynamic recrystallization and deformation mechanisms". In: *Journal of Structural Geology* 27.6, pp. 948–963.

Thielmann, Marcel and Boris JP Kaus (2012). "Shear heating induced lithospheric-scale localization: Does it result in subduction?" In: *Earth and Planetary Science Letters* 359, pp. 1–13.

Thom, CA, RW Carpick, and DL Goldsby (2018). "Constraints on the Physical Mechanism of Frictional Aging from Nanoindentation". In: *Geophysical Research Letters*.

Thom, CA et al. (2017). "Nanoscale Roughness of Natural Fault Surfaces Controlled by Scale-Dependent Yield Strength". In: *Geophysical Research Letters* 44.18, pp. 9299–9307.

Tisato, Nicola et al. (2012). "Experimental investigation of flash weakening in limestone". In: *Journal of Structural Geology* 38, pp. 183–199.

Toy, Virginia G et al. (2009). "The role of pyroxenites in formation of shear instabilities in the mantle: evidence from an ultramafic ultramylonite, Twin Sisters Massif, Washington". In: *Journal of Petrology* 51.1-2, pp. 55–80.

Uchic, Michael D et al. (2004). "Sample dimensions influence strength and crystal plasticity". In: *Science* 305.5686, pp. 986–989.

Urai, Janos L et al. (1986). "Weakening of rock salt by water during long-term creep". In: *Nature* 324.6097, p. 554.

Urai, JL and CJ Spiers (2007). "The effect of grain boundary water on deformation mechanisms and rheology of rocksalt during long-term deformation". In: *Proc. 6th Conf. Mech. Beh. of Salt*, pp. 149–158.

Van Keken, PE et al. (1993). "The effective viscosity of rocksalt: implementation of steady-state creep laws in numerical models of salt diapirism". In: *Tectonophysics* 225.4, pp. 457–476.

Wallis, David et al. (2016). "Geometrically necessary dislocation densities in olivine obtained using high-angular resolution electron backscatter diffraction". In: *Ultramicroscopy* 168, pp. 34–45.

Warren, Jessica M and Greg Hirth (2006). "Grain size sensitive deformation mechanisms in naturally deformed peridotites". In: *Earth and Planetary Science Letters* 248.1-2, pp. 438–450.

Wawersik, WR and DH Zeuch (1986). "Modeling and mechanistic interpretation of creep of rock salt below 200 C". In: *Tectonophysics* 121.2-4, pp. 125–152.

Zhong, Shijie and AB Watts (2013). "Lithospheric deformation induced by loading of the Hawaiian Islands and its implications for mantle rheology". In: *Journal of Geophysical Research: Solid Earth* 118.11, pp. 6025–6048.

INDEX